https://doi.org/10.5194/egusphere-2025-5804
Preprint. Discussion started: 2 February 2026

Exploring atmospheric CH_4 monitoring network expansion in Italy using inverse modelling

Joël Thanwerdas[1], Paolo Cristofanelli[2], Angela Fiore[3], Rianne Dröge[4], Sophie Van Mil[4], Yohanna Villalobos[5], Zhendong Wu[6], and Dominik Brunner[1]

[1]Empa, Swiss Federal Laboratories for Materials Science and Technology, Dübendorf, Switzerland
[2]National Research Council of Italy—Institute of Atmospheric Sciences and Climate (CNR-ISAC), Bologna, Italy
[3]Italian Institute for Environmental Protection and Research (ISPRA), Rome, Italy
[4]TNO, Air Quality and Emissions Research, Utrecht, Netherlands
[5]Department of Physical Geography and Ecosystem Science, Lund University, Lund, Sweden
[6]ICOS Carbon Portal, Department of Physical Geography and Ecosystem Sciences, Lund University, Lund, Sweden

Correspondence: Joël Thanwerdas (joel.thanwerdas@empa.ch)

Abstract. Top-down approaches using inverse modelling provide valuable complementary information to national methane emission inventories, which are primarily based on bottom-up methods. Here we focus on Italy, where methane is currently monitored at five stations that belong to the Integrated Carbon Observation System (ICOS). Compared to other countries, Italy remains poorly covered by ICOS atmosphere sites, resulting in weak observational constraints on methane fluxes. In this study, we assess the potential expansion of Italy's ICOS network using Observation System Simulation Experiments (OSSEs) and inverse modelling. Eight candidate sites were identified, selected either from existing non-ICOS monitoring stations or from proposed future locations. To conduct the OSSEs, we use the ICON-ART model coupled with the Community Inversion Framework (CIF). We design a set of network expansion scenarios to evaluate the potential of each candidate station to improve emission constraints and include four additional scenarios to quantify the contribution of existing and idealized networks. To reduce the influence of randomness, multiple "emission truth" scenarios are constructed. Among all candidates, Chieti (CHI; 42.2°N, 14.7°E) and Mount Venda (VND; 45.3°N, 11.7°E) emerge as the most effective additions, with Chieti showing a slight overall advantage. Chieti enhances constraints mainly in Central and Southern Italy, while Mount Venda is particularly effective in Northern Italy, where most anthropogenic methane emissions originate. The framework developed here can be readily applied to other countries aiming to optimize their atmospheric measurement networks and to improve constraints on greenhouse gas emissions.

1 Introduction

The Paris Agreement (PA) under the United Nations Framework Convention on Climate Change (UNFCCC) commits nations to limit global temperature rise to below 2 °C compared to pre-industrial levels (UNFCCC, 2015). Countries that are parties to the UNFCCC must report their greenhouse gas (GHG) emissions, fostering transparency, tracking progress, and promoting international cooperation on climate change. Currently, countries report their emissions using bottom-up inventories, which are based on 1) socioeconomic and environmental data and 2) source-specific emission factors. However, compiling these

https://doi.org/10.5194/egusphere-2025-5804
Preprint. Discussion started: 2 February 2026

inventories is resource-intensive, time-consuming, and typically completed with a two-year delay. The quality of reporting also varies significantly between nations due to differences in resources and technical capabilities. To support the PA's mitigation goals, top-down monitoring systems can complement bottom-up inventories, as recognized by the 2019 Refinement to the 2006 IPCC Guidelines for National Greenhouse Gas Inventories (Calvo Buendia et al., 2019).

Top-down methods, also known as inverse modeling, rely on atmospheric transport models and data assimilation techniques. By assimilating observed atmospheric GHG concentrations through statistical approaches (e.g., Bayesian frameworks), these methods can help reconcile bottom-up inventories (prior estimates) with atmospheric observations, resulting in refined posterior estimates of emissions. Top-down methods provide independent, consistent, and timely information at global, regional, national, and sub-national scales (Janssens-Maenhout et al., 2020; Bergamaschi et al., 2018). However, the quality of these top-down estimates heavily relies on the coverage and the precision of atmospheric measurements. Observational in-situ networks should therefore be carefully designed to minimize uncertainties and improve our ability to track the temporal evolution of GHG fluxes at regional and national scales.

To address the needs for better measuring the atmospheric GHG concentrations as well as the fluxes between the atmosphere, the land surface and the oceans, the European Union has created the Integrated Carbon Observation System (ICOS; Heiskanen et al., 2022). It is a world-class observational network that provides high-quality, standardized and open data from about 180 measurement stations of three different types, atmosphere, ecosystem, and ocean, across 16 European countries. Since its establishment in the early 2010's, ICOS has been continuously expanding its observation network. Today, the atmosphere network consists of 47 stations (39 labeled and 8 candidate stations) measuring GHG atmospheric concentrations across Europe.

Among the well-mixed GHGs, anthropogenic methane (CH_4) has the second largest influence on global warming. This gas has a global warming potential approximately 80 times higher than carbon dioxide (CO_2) over a 20-year period (Forster et al., 2021) and also plays a crucial role in atmospheric chemistry, influencing ozone formation and hydroxyl radical (OH) concentrations. Hence, reducing CH_4 emissions can yield rapid climate and air pollution benefits, which emphasizes the need for accurate quantification of its sources and sinks (Saunois et al., 2025), and making it a key target for the climate mitigation efforts requested by the PA. Bottom-up estimates show that Italy is a significant CH_4 emitter in Europe, with major contributions from agriculture (enteric fermentation and manure management), waste management and energy (Romano et al., 2024). Complementing these estimates with inverse modelling requires the observational network in Italy to provide a good coverage of the country. At present, five ICOS sites are monitoring continuously CH_4 in Italy: Plateau Rosa (PRS; 45.9° N, 7.7° E), Ispra (IPR; 45.8° N, 8.6° E), Potenza (POT; 40.6° N, 15.7° E), Monte Cimone (CMN; 44.2° N, 10.7° E) and Lampedusa (LMP; 35.5° N, 12.6° E). PRS, CMN, IPR have been measuring atmospheric CH_4 in Northern Italy since 2005, 2008, and 2017, respectively, while POT, which recently began monitoring CH_4 (Lapenna et al., 2025), is expected to provide valuable coverage in Southern Italy in the future. LMP is a marine remote site located on Lampedusa island, deep in the Mediterranean sea and distant from continental Italy, monitoring since 2008. More stations, introduced in Sect. 2.4, are also monitoring CH_4 in Italy, although they are not part of the ICOS network.

Here, we conduct Observation System Simulation Experiments (OSSEs) with the Eulerian model ICON-ART to assess the effectiveness of the current monitoring network in Italy and evaluate potential expansions. This work complements a re-

https://doi.org/10.5194/egusphere-2025-5804
Preprint. Discussion started: 2 February 2026

cent study that investigated the same expansion in Italy for CO_2 monitoring using Lagrangian modelling (Villalobos et al., 2025). Both studies are conducted within the framework of the EU-HORIZON AVENGERS project. In the context of inverse modelling, OSSEs involve generating synthetic "true" emissions based on prior knowledge of their magnitude and associated uncertainties. These true emissions are then used to produce corresponding synthetic atmospheric observations using a transport model. We perform inversions by assimilating these synthetic observations representing the true atmospheric state to optimize the prior emission estimates. With each assimilated observation, the optimized emissions are expected to converge toward the true emissions. The degree of agreement between optimized and true emissions depends on the quality, spatial and temporal coverage, and quantity of observations in the network. OSSEs therefore provide a valuable framework to evaluate the impact of adding measurement sites, helping to identify optimal locations and compare different network expansion scenarios. OSSEs have previously been used in inverse modelling to assess the potential impact of existing or new surface stations (e.g., Takele Kenea et al., 2024; Park and Kim, 2020; Wang et al., 2018; Kaminski and Rayner, 2017; Wu et al., 2016; Hungershoefer et al., 2010; Baker et al., 2010) or satellites (e.g., Santaren et al., 2021; Yu et al., 2021; Basu et al., 2016; Bloom et al., 2016; Nickless et al., 2015; Ziehn et al., 2014; Shiga et al., 2014; Miyazaki et al., 2011; Villani et al., 2010; Edwards et al., 2009; Meirink et al., 2006; Rayner et al., 1996). In this work, alongside exploring the expansion of the Italian observational network, we build upon previous work and introduce a methodology that is both easily reproducible and adaptable to any country with Eulerian modelling. Furthermore, we employ the Community Inversion Framework (CIF; Berchet et al., 2021) to perform our inversions. Most of the Eulerian models used in the inversion community have now been coupled to CIF and our methodology can therefore be easily applied with these models. This methodology also addresses an important caveat commonly found in the studies mentioned above: the impact of randomness and truth selection. Because the chosen truth is just one of many potential realities, the results can be artificially influenced toward a specific station when the prior and truth are already in good agreement around the station before the inversion. To mitigate such an effect, we adopt an ensemble of truth scenarios.

Section 2 introduces the transport model, inversion system, input data, and network scenarios considered in this study. It also outlines the generation of synthetic data and the choice of true emission data. Section 3 presents the results, while Section 4 addresses the caveats and limitations of the applied methodology.

2 Methods

Here, we describe the transport model, inversion framework, and input data used to generate the prior estimates, along with the network scenarios considered in this study.

2.1 ICON-ART model

The Icosahedral Nonhydrostatic (ICON) weather and climate model (Zängl et al., 2015) is a collaborative effort between the Deutscher Wetterdienst (DWD), the Max Planck Institute for Meteorology (MPI-M), the Deutsches Klimarechenzentrum (DKRZ), the Karlsruhe Institute of Technology (KIT), and the Center for Climate Systems Modeling (C2SM) in Switzerland. Its goal is to develop a unified, next-generation global system for numerical weather prediction (NWP) and climate modeling.

https://doi.org/10.5194/egusphere-2025-5804
Preprint. Discussion started: 2 February 2026

ICON became operational within DWD's and MeteoSwiss' forecasting systems in 2015 and 2024, respectively. Notably, ICON was made available as open-source software to expand its user and developer community in February 2024. To incorporate atmospheric chemistry and aerosol processes, ICON is extended by the Aerosols and Reactive Trace gases (ART) module, developed and maintained by KIT (Hoshyaripour et al., 2025; Schröter et al., 2018; Rieger et al., 2015). This combination forms the ICON-ART model, a non-hydrostatic Eulerian chemical transport model that includes emissions, transport, gas-phase chemistry, and aerosol dynamics in both the troposphere and stratosphere. ICON-ART uses an icosahedral grid that can cover the entire globe or be restricted to limited areas, ranging in horizontal resolution from several degrees down to a few kilometers.

For the present study, the model is configured with a horizontal resolution of 26 km (approximately 0.3°) over Italy and its surroundings (2°N – 24°N, 32°E – 54°E), consisting of 5048 grid cells (see Fig. 1). Vertically, the model extends from the surface up to 23 km with 60 levels, using a height-based, terrain-following coordinate system.

Meteorological variables are computed online by the ICON model. In this setup, key prognostic variables (including wind speed, specific humidity, density, virtual potential temperature, and Exner pressure), are weakly nudged toward ERA5 reanalysis data (Hersbach et al., 2023, 2017) from the ECMWF, available at a 3-hourly temporal resolution. This nudging helps maintain the model's realism and prevents significant drift from observed atmospheric conditions. ERA5 data also provide the model's initial state. We simulate the year 2018 to be consistent with Villalobos et al. (2025).

Emission fields for transported species are processed via the Online Emissions Module (OEM; Jähn et al., 2020), integrated within ART. Output files of instantaneous concentrations are saved hourly and later interpolated in time, height, and space to derive model equivalents of observational data.

2.2 Community Inversion Framework

The Community Inversion Framework (CIF; Berchet et al., 2021) is an inversion system that has been designed to bring together the different inversion methods (analytical, variational and ensemble) and transport models used in the inversion community. It is built as an open-source, well documented, highly modular multi-model inversion framework written in Python that facilitates the comparison of (1) inversion methods and (2) transport models. CIF has proved to be accurate and computationally performant over the past years (Wittig et al., 2023; Savas et al., 2023; Remaud et al., 2022; Thanwerdas et al., 2024, 2022b, a)

We employ the ensemble square root filter (EnSRF) algorithm implemented in CIF to perform the inversions presented in this study. This algorithm has recently been improved and is thoroughly described in Thanwerdas et al. (2025). Briefly, an ensemble of vectors is used to represent the probability distribution of the control vector, which contains all the variables that we wish to optimize (e.g., fluxes, background concentrations, etc). Each member of the ensemble is attached to a different tracer transported by the model. After running simulations with this ensemble of tracers, the resulting ensemble of output concentrations is used to optimize the control vector to minimize the mismatch with the assimilated observations of atmospheric concentrations. In this study, the variables being optimized are scaling factors applied to the fluxes at the model's horizontal resolution.

https://doi.org/10.5194/egusphere-2025-5804
Preprint. Discussion started: 2 February 2026

The full assimilation time period is partitioned into several windows of finite length. For each window, a single scaling factor is associated with each optimized variable (e.g., flux emitted in a cell of the horizontal domain). Scaling factors within the window are optimized using both the observations from the current window and the observations from a fixed number (lag) of subsequent windows. Covariance localization is also applied to mitigate spurious long-range correlations that tend to appear in the ensemble. More details about the exact setup employed for this study is provided in Sect 2.8.

2.3 Input data

The prior information is based on several high-quality datasets, which are merged into two categories of emissions: anthropogenic and natural. Total, anthropogenic and natural emissions are shown in Fig. 1.

2.3.1 Anthropogenic and natural fluxes

Except for fire emissions, all anthropogenic CH_4 fluxes are based on the TNO-AVENGERS inventory (Dröge et al., 2024). The TNO-AVENGERS inventory consist of national gridded inventories of Germany, Italy, the Netherlands, Sweden and Switzerland nested within the TNO-GHGco_v7 inventory for the other European countries. The approach to prepare the TNO-GHGco_v7 inventory is similar to CAMS-REG_v4 (Kuenen et al., 2022), but now also includes N_2O emissions of all sectors and CO_2, CH_4 and N_2O emissions from the LULUCF sector. The yearly spatial distribution of emissions is provided at a horizontal resolution of $0.05° \times 0.1°$ over Europe. Additionally, hour-of-day, day-of-week and month-of-year temporal scaling factors are also included in the dataset and can be applied on the spatial distribution to create an hourly emission dataset. Fire emissions are based on the Global Fire Emissions Database version 4s (GFED4s; van der Werf et al., 2017) and are provided at a monthly resolution and a horizontal resolution of $0.25° \times 0.25°$. According to this dataset, about 78% of the anthropogenic CH_4 was emitted by the agriculture (mainly in Northern Italy) and waste sectors (mainly in Southern Italy) in 2018. The remaining emissions were mostly released by fugitive sources (mainly in Northern Italy) and biofuel burning (spread over the country).

We use a dataset produced with the model LPJ-GUESS (Lund-Potsdam-Jena General Ecosystem Simulator, version 4.1, revision 12177, Smith et al., 2001) to represent the soil uptake emissions from peatlands and inundated wetlands. LPJ-GUESS is a process-based dynamic vegetation-terrestrial ecosystem community model designed for regional or global studies of land surface processes. It has been developed by Lund University in a collaboration involving the Potsdam Institute for Climate Impact Research and the Max-Planck Institute for Biogeochemistry, Jena. This dataset is provided at daily temporal resolution and spatial resolution of 0.5°.

For other natural sources, we rely on bottom-up estimates compiled for the inversions conducted as part of the Global Methane Budget (Saunois et al., 2020). These include the datasets for oceanic sources (including geological offshore and hydrate emissions), onshore geological sources and termites described in Saunois et al. (2020). These datasets are available at monthly temporal resolution and $0.1° \times 0.1°$spatial resolution.

https://doi.org/10.5194/egusphere-2025-5804
Preprint. Discussion started: 2 February 2026

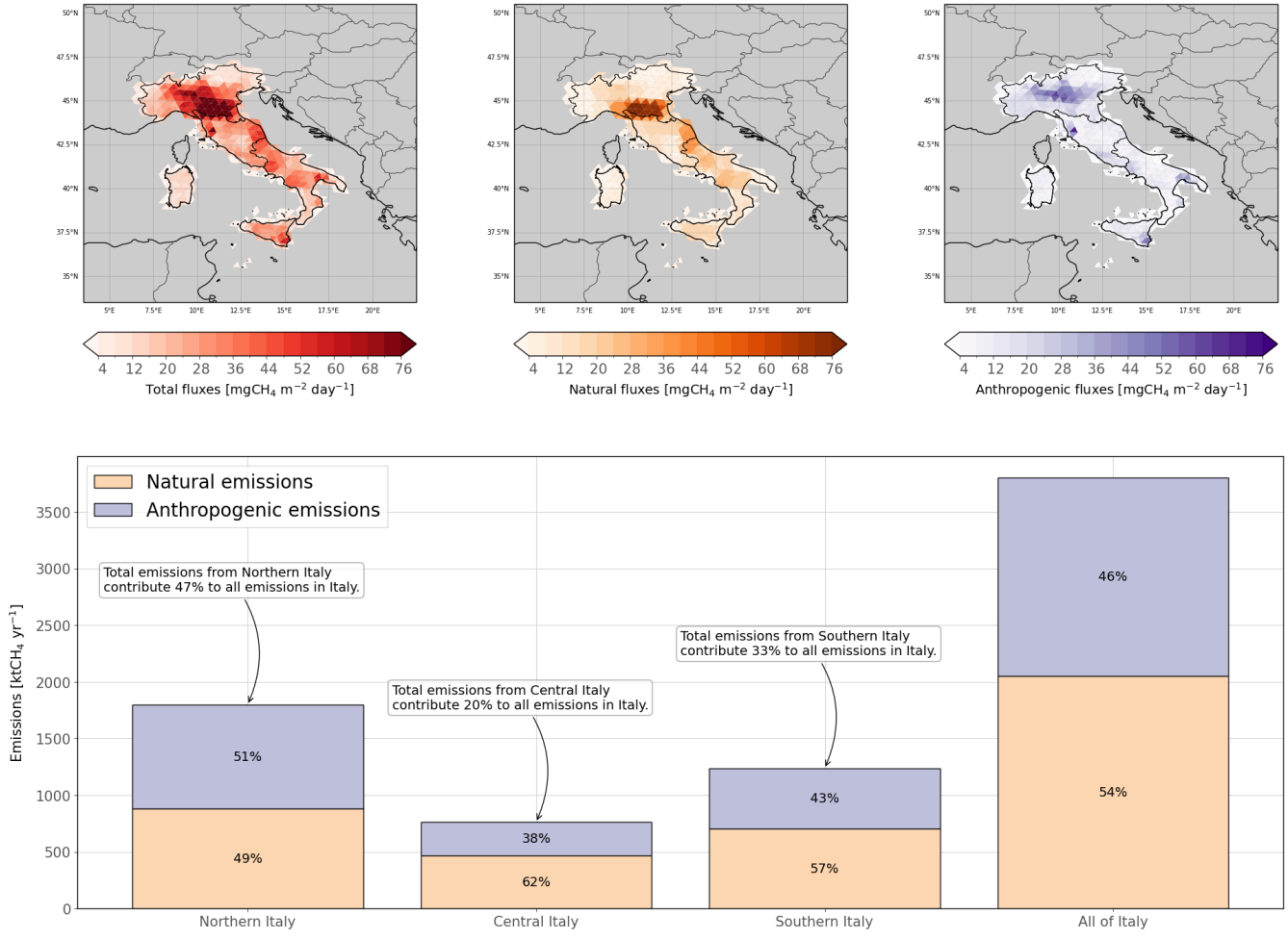

Figure 1. Spatial distribution of total, natural and anthropogenic fluxes in Italy (upper panels) and contributions of natural and anthropogenic emissions to total emissions in Northern, Central, Southern, and all of Italy (lower panel). Numbers displayed at the center of bars represent the contribution of each category to the total emissions in a specific region.

2.3.2 Background concentrations

Initial conditions and lateral boundary conditions for CH_4 mole fractions are derived from the CAMS global inversion-optimized CH_4 concentration product v21r1 (Segers, 2022). The data are based on surface observations only and are provided at a horizontal resolution of $3.0° \times 2.0°$ and at a 6-hourly temporal resolution.

2.4 Candidate stations

For selecting candidate stations for the extended ICOS network, we consider 8 locations from Italy's existing or planned monitoring infrastructure:

https://doi.org/10.5194/egusphere-2025-5804
Preprint. Discussion started: 2 February 2026

- Mount Venda (VND, 45.3° N, 11.7°E). It is a proposed new site intended to improve constraints on emissions in the high-emission Po Valley region. A preliminary study investigated the possibility of installing a GHG sampling inlet at a transmission tower on the summit of Mount Venda (570 m), in the eastern Po Valley. However, this remains at the planning stage due to funding limitations.

- Chieti (CHI; 42.2° N, 14.7°E). This site has been recently established. It is operated by the University of Chieti and located on the Adriatic coast, and is expected to begin measuring GHGs in 2025–2026.

- Lecce (ECO; 40.3° N, 18.1°E). This site is located near the urban area of Lecce (population 94,377), about 10 km from the South Adriatic Sea. CH_4 measurements were continuously performed from 2015 to 2017 (Dinoi, 2025) by the National Research Council of Italy (CNR) – Institute for Atmospheric Science and Climate (ISAC).

- Lamezia Terme (LMT; 38.9° N, 16.2°E). This site is located along the Tyrrhenian Sea coastline, and CH_4 measurements have been conducted since 2015 by CNR-ISAC (Malacaria et al., 2025).

- Capo Granitola (CGR; 37.6° N, 12.7°E). This site is located on the southern coast of Sicily facing the Strait of Sicily, and is jointly operated by CNR-ISAC and CNR-IAS (the Institute for the Study of Anthropic Impact and Sustainability in the Marine Environment). In situ CH_4 atmospheric observations were carried out here over the period 2015–2019 and 2022–2023 (Cristofanelli et al., 2025), and are expected to resume in 2026.

- Madonie – Piano Battaglia (MDN; 37.9° N, 14.0°E). This site is located in a mountainous area in northern Sicily. Since 2005, ENEA (Italian National Agency for New Technologies, Energy and Sustainable Economic Development) has been performing weekly flask sampling (Sferlazzo et al., 2025).

- Monte Curcio (CUR; 39.3° N, 16.4°E). It is a mountain station located in the heart of the Calabria region, managed by the CNR-IIA (Institute of Atmospheric Pollution Research). Hourly CH_4 data are available only from 2015 to 2017 (Bencardino, 2025), but the station remains active.

- Col Margherita (MRG; 46.8° N, 11.8°E). This observatory is located on the southern slope of the Eastern Alps, within the Dolomites. It is representative of the synoptic conditions of the south-facing Eastern Alps, where there is no similar station. The observatory is equipped with a complete meteorological station, an ozone analyser and a total gaseous mercury analyser, but the station does not monitor CH_4 concentrations.

ECO, LMT, CGR, CUR, MDN, and MRG are not part of ICOS but actively contribute to the regional Global Atmospheric Watch (GAW) programme of the World Meteorological Organization (WMO). Further information about these stations is provided in Table A1. Locations are displayed on a spatial map in Fig2 (Scenario 11).

2.5 Network scenarios

This study evaluates twelve atmospheric measurement network scenarios encompassing Italy and its neighboring countries. The primary goal is to determine which candidate stations, introduced in Sect. 2.4, would provide the greatest benefit for

https://doi.org/10.5194/egusphere-2025-5804
Preprint. Discussion started: 2 February 2026

constraining emissions in Italy. It results in eight different scenarios, each featuring one of the candidate stations. In addition, several supplementary network scenarios are considered to assess the contribution of existing networks and to estimate the optimal achievable constraints on Italian emissions. The twelve scenarios, displayed in Fig. 2, are outlined as follows:

- **Scenario 1** includes only ICOS sites located in countries bordering Italy. This configuration serves to assess the ability of external networks to constrain emissions originating within Italy.
- **Scenario 2**, referred to as the base network, expands on Scenario 1 by incorporating ICOS sites located within Italy.
- **Scenarios 3 through 10** each evaluate the impact of adding a single additional station to the base network among the candidate stations. Specifically, the added stations are:
  - **Scenario 3**: VND
  - **Scenario 4**: CHI
  - **Scenario 5**: ECO
  - **Scenario 6**: LMT
  - **Scenario 7**: CGR
  - **Scenario 8**: MDN
  - **Scenario 9**: CUR
  - **Scenario 10**: MRG
- **Scenario 11** combines the base network with all eight stations evaluated individually in Scenarios 3–10.
- **Scenario 12** builds on Scenario 11 by further including all 16 Italian ICOS ecosystem stations, which are described in Table A3, to explore the full potential of an optimized measurement network in Italy.

These scenarios enable a systematic evaluation of how different network configurations influence the capacity to monitor and constrain GHG emissions across the region.

2.6 Characteristics of synthetic observations

Synthetic observations generated with the transport model ICON-ART are assimilated by the inversion system to refine prior estimates and to assess the potential of each candidate station for constraining emissions. Conducting robust OSSEs to identify the most suitable stations for network expansion requires producing synthetic observations with times and locations that closely replicate those of real-world measurements.

For existing stations, we use synthetic observations matching the locations and times of the real observations compiled in version 9.2 of the ICOS ObsPack CH_4 data product (ICOS RI et al., 2024). This dataset includes continuous measurements from 66 stations across Europe collected between 1984 and 2024, encompassing both ICOS and non-ICOS facilities. Within

https://doi.org/10.5194/egusphere-2025-5804
Preprint. Discussion started: 2 February 2026

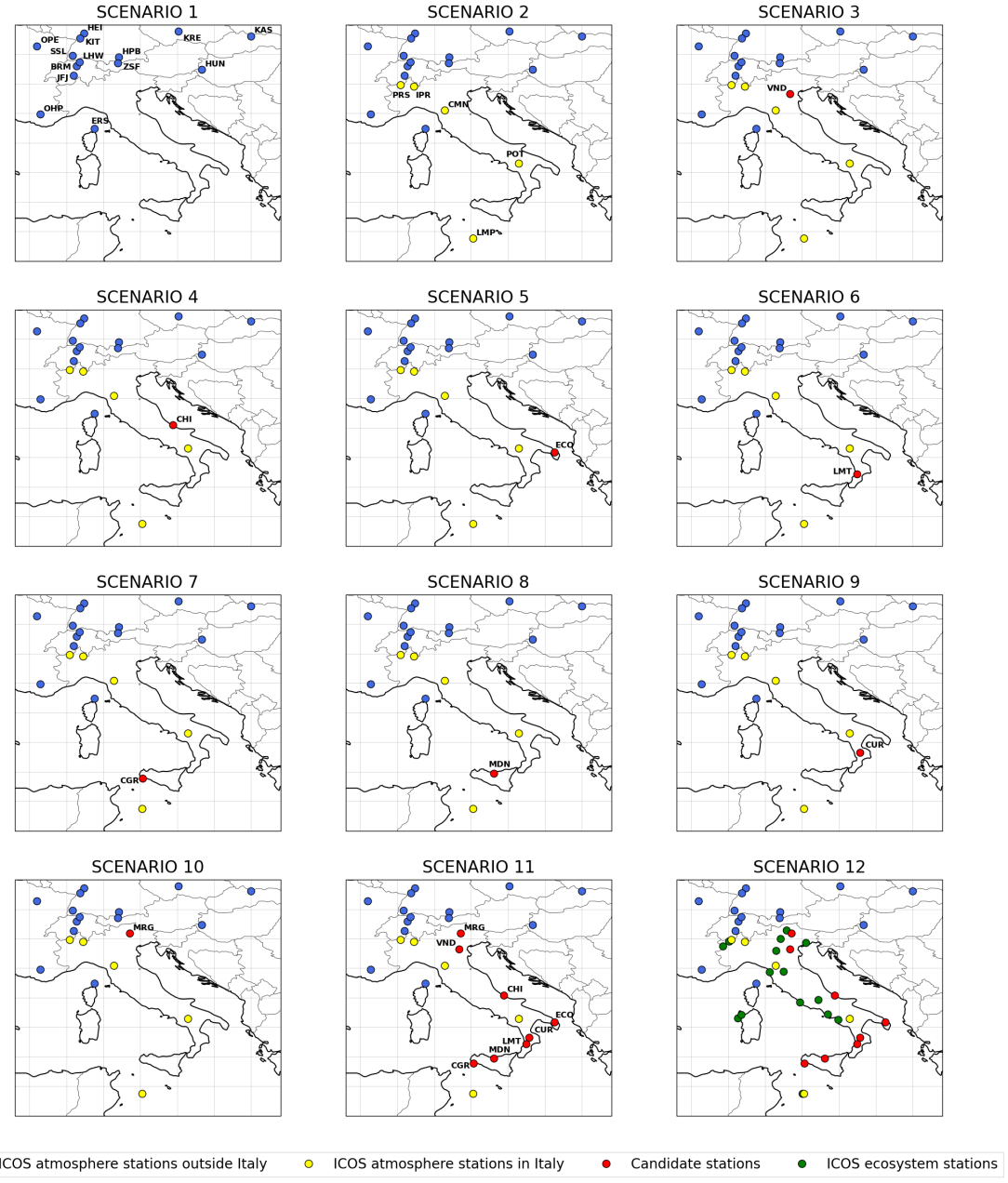

Figure 2. Description of the sites featured in the twelve atmospheric measurement network scenarios. The blue circles show the neighboring stations, i.e. outside Italy. The yellow circles show the ICOS atmosphere sites in Italy. The red circles show the candidate stations studied in the scenarios 3 through 10. The green circles show the ecosystem ICOS stations. To improve readability, ICOS ecosystem station names are not displayed in scenario 12.

https://doi.org/10.5194/egusphere-2025-5804
Preprint. Discussion started: 2 February 2026

the temporal and spatial bounds of our experiments, data from 19 stations are available (blue circles in Fig. 2), with detailed station information provided in Table A2.

For candidate and ecosystem stations, we assume hourly measurements taken at a sampling height of 2 m for mountain sites and 100 m (i.e., from tall towers) for lowland sites. VND represents a special case, as measurements there would be collected at 50 m, from the top of an existing radio-television tower. These specifications are applied in the generation of our synthetic observations.

2.7 Generation of true emissions and synthetic observations

To generate synthetic observations with the ICON-ART transport model, we first sample a set of "true" scaling factors (representing the ratio of true to prior emissions) for each grid cell in the ICON-ART domain ($c = 5048$ cells), following the approach described by Thanwerdas et al. (2025). We briefly present it here.

The true scaling factors are sampled from a normal distribution with a prior-error covariance matrix $\mathbf{B}$. We account for both spatial and temporal correlations. For spatial correlations, we first construct a correlation matrix based on an exponential decay function, $e^{-\frac{d_{i,j}}{L}}$, where $d_{i,j}$ denotes the great-circle distance between cells i and j, and L is the spatial correlation length. We then scale this matrix by the chosen variance to obtain the spatial covariance matrix. A similar procedure is applied to introduce temporal correlations, replacing spatial distances with the time interval between similar optimized variables (i.e., corresponding to the same cell), normalized by the temporal correlation length. The full covariance matrix, accounting for both spatial and temporal correlations, is built using Kronecker products. Using the singular value decomposition (SVD) of the full matrix $\mathbf{B}$, we generate an ensemble of spatially and temporally correlated scaling factors.

In line with the recommendations of Szénási et al. (2021) and anthropogenic correlation lengths estimated by TNO for Italy (Super et al., 2020), we adopt a spatial correlation length of 200 km for natural fluxes and 100 km for anthropogenic fluxes, considering no correlation for fossil fuel emissions and a correlation length of 150 km for agriculture and waste emissions. To determine the appropriate variance for each scaling factor, we compute the country-scale uncertainty for both flux types using the specified correlation lengths and a range of relative variances (50%, 100%, 150%, 200%). Our analysis suggests that relative variances of approximately 150% are required for both natural and anthropogenic fluxes to match the country-scale uncertainties reported by TNO (for anthropogenic fluxes) and by Szénási et al. (2021) (for both flux types in Italy). However, applying relative variances above 100% within a Gaussian framework increases the risk of generating negative flux values during the inversion. To balance realistic uncertainty representation with these technical constraints, we adopt a relative variance of 100% for both flux categories. Although it results in a prior uncertainty that is slightly underestimated compared to existing estimates, it should not affect the conclusions of this study as we use an inversion set-up where true uncertainties are considered to be perfectly known. Note that, due to the shorter correlation length applied to anthropogenic fluxes, it results in a lower country-scale uncertainty for anthropogenic emissions compared to natural ones.

To account for a potential temporal variability of the mismatch between prior and true estimates, we generate a new set of true scaling factors for each 10-day period throughout the year 2018. To maintain seasonal coherence, we impose a temporal correlation using an exponential decay with a temporal correlation length of three months. The resulting scaling factors,

https://doi.org/10.5194/egusphere-2025-5804
Preprint. Discussion started: 2 February 2026

averaged over 2018, are shown in Fig. 3. The perturbed fluxes used as the synthetic "truth" are obtained by applying these scaling factors to the corresponding prior fluxes. The selected values for prior relative variances and for spatial and temporal correlations lengths are summarized in Table 1.

Table 1. Selected values for prior relative variances and for spatial and temporal correlation lengths to build the prior-error covariance matrix **B**.

	Prior relative variance	Spatial correlation length	Temporal correlation length
Anthropogenic	100%	100 km	3 months
Natural	100%	200 km	3 months

Finally, we run a 1-year forward simulation over 2018 with the perturbed fluxes. After this forward simulation, the simulated values matching the time and locations of the observations (for existing stations) or pseudo-observations (for candidate and ecosystem stations) introduced in Sect. 2.6 are stored. These simulated values are then treated as the new observations to be assimilated in the experiments presented in the next section. Additionally, to mimic realistic model-data mismatch uncertainties arising from both modelling and measurement errors, we perturb them with random values drawn from a Gaussian distribution with a mean of 0 and a standard deviation of 20 ppbv. This corresponds to the typical model-data mismatch calculated in Steiner et al. (2024b) with ICON-ART runs at a resolution of 26 km.

Model–data mismatch plays a critical role in atmospheric inversions, as it directly affects the assimilation weights assigned to each observation and, consequently, the inversion outcomes. Assigning a uniform model–data mismatch across all stations implies equal trust in all observations, regardless of site-specific conditions. While this assumption is a simplification, it serves a useful purpose in the initial phase of our study: it allows us to isolate and evaluate the influence of station location on the inversion results. However, in real-data applications, model–data mismatch is inherently site-dependent. It reflects the degree of confidence in the model's ability to accurately simulate concentrations at a given location, which can vary due the model's ability to capture local atmospheric dynamics and local sources, given the complexity of the surrounding environment. In Sect. 3.5, we present a refined, station-specific estimation of model–data mismatch and analyze its impact on the inversion results.

To cover a wider range of emission uncertainties, we replicate this methodology five times to generate five different sets of synthetic observations based on five different sets of true fluxes (hereinafter called truth scenario). The importance of using different truths for an OSSE is illustrated and discussed in Sect. 3.2.

2.8 Inversion setups

For each designed network and each set of true fluxes and perturbed observations, we run a 1-year inversion (i.e. 12 network scenarios x 5 truth scenarios = 60 inversions) spanning 2018 with the EnSRF mode of CIF-ICON-ART. Following the conclusions of Thanwerdas et al. (2025), we use the following CIF settings to run all the inversions:

- Window length = 10 days

https://doi.org/10.5194/egusphere-2025-5804
Preprint. Discussion started: 2 February 2026

- Number of lags = 2
- Localization function is an exponential function
- Localization length = 600 km

To build the prior error-covariance matrix $\mathbf{B}$, relative variances and spatial and temporal correlations are prescribed to match the values used in generating the true scaling factors (see Table 1).

2.9 Evaluation metrics

We use two different metrics to quantitatively compare network designs: error reduction and uncertainty reduction. Here, we define them.

2.9.1 Error reduction (ER)

The error reduction (ER) quantifies the agreement between the optimized fluxes and the true fluxes. It is defined by:

$$\mathrm{ER}(k,t) = 1 - \frac{\boldsymbol{e_a}(k,t)}{\boldsymbol{e_b}(k,t)} = 1 - \frac{|\boldsymbol{x_a}(k,t)\cdot\boldsymbol{F}(k,t) - \boldsymbol{x_t}(k,t)\cdot\boldsymbol{F}(k,t)|}{|\boldsymbol{x_b}(k,t)\cdot\boldsymbol{F}(k,t) - \boldsymbol{x_t}(k,t)\cdot\boldsymbol{F}(k,t)|} \tag{1}$$

Here, $\boldsymbol{x_b}(.)$, $\boldsymbol{x_a}(.)$ and $\boldsymbol{x_t}(.)$ are the vectors representing the prior, posterior, and true scaling factors. In this work, $\boldsymbol{F}(.)$ is either the anthropogenic flux, the natural flux or the sum of them; $\boldsymbol{e_b}(.)$ and $\boldsymbol{e_a}(.)$ are the prior and posterior absolute flux errors, respectively. k and t represent the cells of the model's horizontal grid and the time dimension, respectively. This formula gives a quantity that is time dependent and spatially distributed. A positive ER indicates that the optimized fluxes agree better with the truth than the prior data, whereas a negative ER shows the opposite. We further define the mean error reduction (MER) using time and area-weighted spatial averages of the flux errors,

$$\mathrm{MER}(\mathcal{S},\mathcal{T}) = 1 - \frac{\overline{\boldsymbol{e_a}(k,t)}^{\mathcal{S},\mathcal{T}}}{\overline{\boldsymbol{e_b}(k,t)}^{\mathcal{S},\mathcal{T}}} = 1 - \frac{\sum_{k\in\mathcal{S},\,t\in\mathcal{T}} \boldsymbol{a}(k)\cdot\boldsymbol{e_a}(k,t)}{\sum_{k\in\mathcal{S},\,t\in\mathcal{T}} \boldsymbol{a}(k)\cdot\boldsymbol{e_b}(k,t)} \tag{2}$$

Here, $\mathcal{S}$ and $\mathcal{T}$ denote the spatial and temporal domains, respectively. $\mathcal{S}$ may represent the spatial extent (the entire domain or a region in it), while $\mathcal{T}$ refers to the temporal extent (the full year or a specific season). $a(\cdot)$ denotes the area of a given grid cell. In this study, we consider the entire country and three aggregated regions.

The aggregation is based on the five Eurostat NUTS (Nomenclature of Territorial Units for Statistics) regions of Italy: Northern-West, Northern-East, Central, Southern, and Insular Italy. For our analysis, we combine the two northern regions into a single Northern Italy and merge Insular Italy with Southern Italy, resulting in three regions of comparable area. This division of the entire domain facilitates the quantification of spatial heterogeneity of our results.

It is important to note that the MER does not reflect improvements in domain-total fluxes, as it is based on the sum of absolute errors rather than net differences. Reductions in domain-total flux error can be misleading, as they may result from compensating errors across spatial or temporal domains. In contrast, a high MER reflects a consistent and widespread agreement between posterior and true fluxes, offering a more robust measure of overall inversion performance. MER can be calculated for different regions, seasons, and flux categories. Illustrative examples of ER and MER are provided in Figures 2c and 2d, respectively.

https://doi.org/10.5194/egusphere-2025-5804
Preprint. Discussion started: 2 February 2026

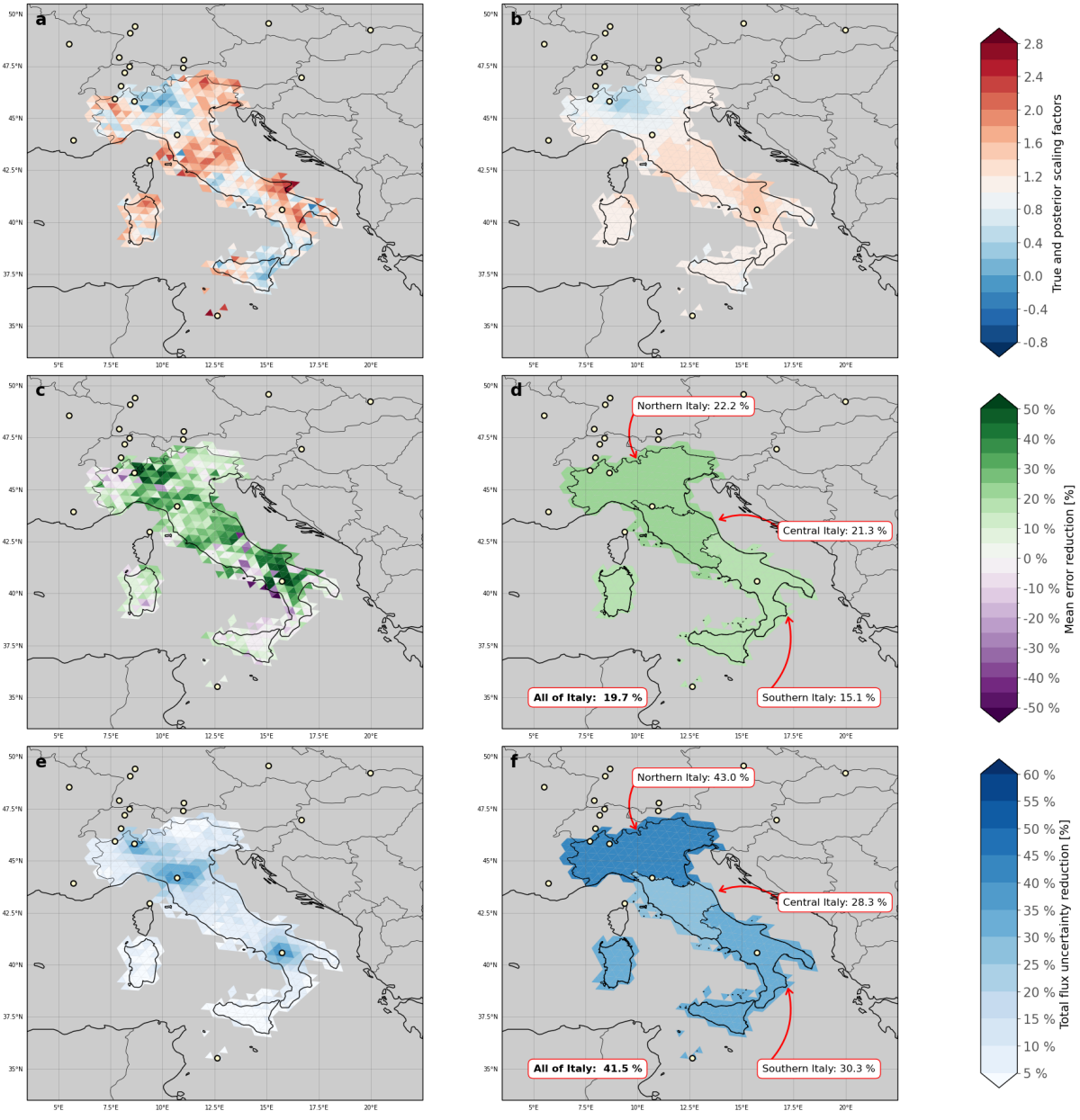

Figure 3. Illustration of the computation of the metrics presented in Sect. 2.9 for scenario 2, and for total CH_4 emissions. We first generate a set of true scaling factors (panel a, averaged here over the full year). Among the five generated truths, we show only the fifth truth here (purple circle in Fig. 5). We start from prior scaling factors all equal to one. After the inversion, we obtain posterior scaling factors (panel b). Based on true, prior and posterior scaling factors, we compute ER (panel c, averaged here over the full year) and annual MER for all Italian regions (panel d). We also compute UR (panel e, averaged here over the full year) and annual TUR for the different Italian regions (panel f).

https://doi.org/10.5194/egusphere-2025-5804
Preprint. Discussion started: 2 February 2026

2.9.2 Uncertainty reduction (UR)

For each cell of the horizontal domain, we define the uncertainty reduction (UR) as the reduction in the ratio of posterior to prior uncertainties,

$$\mathrm{UR}(k,t) = 1 - \frac{\boldsymbol{\sigma_a}(k,t)}{\boldsymbol{\sigma_b}(k,t)} \tag{3}$$

where $\boldsymbol{\sigma_b}(.)$ and $\boldsymbol{\sigma_a}(.)$ denote the vectors representing the prior and posterior standard deviations of scaling factors, respectively. We further define the total flux uncertainty reduction (TUR) as the uncertainty reduction of the domain-total flux (e.g., all of Italy or a specific region in Italy).

$$\mathrm{TUR}(\mathcal{S},\mathcal{T}) = 1 - \sqrt{\frac{\boldsymbol{f_a}^{\mathcal{S},\mathcal{T}}\mathbf{A}(\boldsymbol{f_a}^{\mathcal{S},\mathcal{T}})^T}{\boldsymbol{f_b}^{\mathcal{S},\mathcal{T}}\mathbf{B}(\boldsymbol{f_b}^{\mathcal{S},\mathcal{T}})^T}} \cdot \frac{\sum_{k\in\mathcal{S},t\in\mathcal{T}} \boldsymbol{f_b}(k,t)}{\sum_{k\in\mathcal{S},t\in\mathcal{T}} \boldsymbol{f_a}(k,t)} \tag{4}$$

Here, $\mathcal{S}$ and $\mathcal{T}$ also denote the spatial and temporal domains, respectively. $\mathbf{B}$ and $\mathbf{A}$ denote the prior-error and posterior-error flux covariance matrices. $\boldsymbol{f_b}^{\mathcal{S},\mathcal{T}}$ and $\boldsymbol{f_a}^{\mathcal{S},\mathcal{T}}$ are the vectors containing the prior and posterior fluxes multiplied by the area, respectively, where the entries outside the domains $\mathcal{S}$ and $\mathcal{T}$ have been set to zero. Note that we divide the standard deviations, calculated from $\mathbf{B}$ and $\mathbf{A}$, by the corresponding domain-total flux in order to compare relative rather than absolute uncertainties. Using absolute uncertainties can yield negative uncertainty reductions when the posterior flux estimate is substantially larger than the prior estimate.

TUR can be calculated for different regions, seasons, and flux categories. Although the two metrics MER and TUR are related since both depend on the amount of emission signal detected by the station, a high TUR does not necessarily imply a high MER. If the signal originates from many directions and spans a broad region, the TUR will likely be high because the corresponding footprint is wide. However, when the footprint becomes too broad, the system may struggle to pinpoint the exact source of the detected signal and refine properly the source region responsible for the signal, which results in a low MER. This is further discussed in Sect 4.

Illustrations of UR and TUR are provided in Fig. 3e and Fig. 3f, respectively.

3 Results

3.1 Constraining total CH_4 emissions

Figure 4 shows the MER for total CH_4 emissions across four regions (all of Italy, Northern Italy, Central Italy, and Southern Italy) for each network scenario, and averaged over all truth scenarios. In Scenario 1, which includes only neighboring stations, Northern Italy exhibits a moderate constraint with MER, reaching 18%. In contrast, Central Italy shows weaker skill (MER < 15%), while Southern Italy remains essentially unconstrained, with MER as low as 4%.

Including the existing ICOS stations within Italy (Scenario 2) markedly improves the agreement between posterior and true fluxes, raising MER by about 5–10% across all regions.

https://doi.org/10.5194/egusphere-2025-5804
Preprint. Discussion started: 2 February 2026

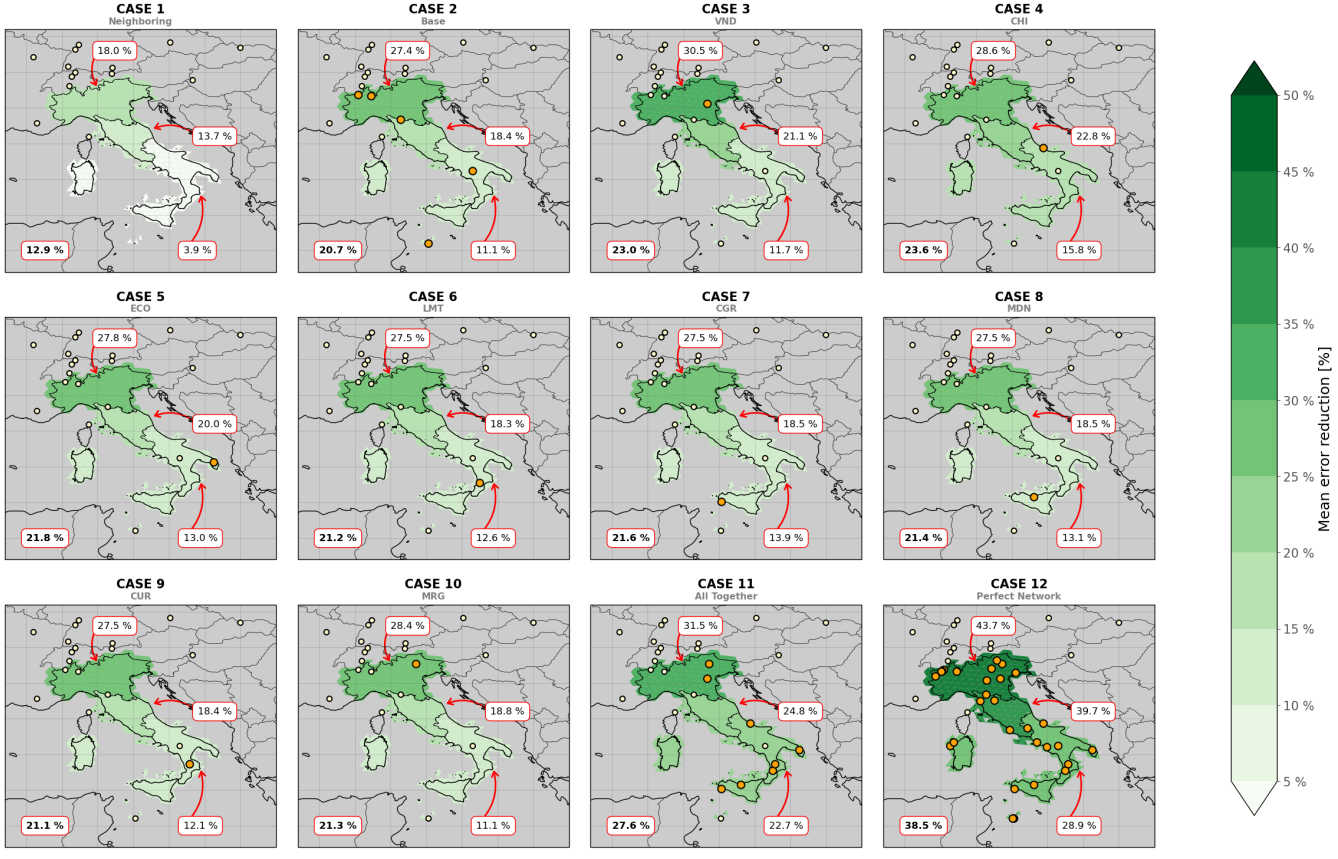

Figure 4. Spatial distribution of MER across Italy, shown separately for the whole country, Northern Italy, Central Italy, and Southern Italy. For each region, the corresponding MER value is annotated in a box placed near its location, while the national value is displayed in the lower-left corner of each panel, in bold. Stations from Scenario 1 are marked with yellow circles, and additional stations introduced in subsequent scenarios are shown as orange circles.

340 Analysis of individual candidate stations indicates that VND and CHI perform best, each achieving 2% higher MER than other sites. VND is particularly effective in Northern Italy, whereas CHI provides stronger constraints in Central and Southern Italy, outperforming all the other candidate stations in those regions. Other stations, such as ECO and CGR, also improve network performance reasonably. While ECO captures information about emissions both in Central and Southern Italy, CGR improves the coverage in Southern Italy.

345 Idealized expansion (i.e., adding all candidate stations in Scenario 11 and the full set of ICOS ecosystem stations in Scenario 12) provides substantial gains, with MER for all of Italy reaching 28% and 39%, respectively. While Northern and Central Italy shows similar results under the ideal scenarios, Southern Italy remains less constrained. This comparatively weak constraint can be attributed to three factors:

https://doi.org/10.5194/egusphere-2025-5804
Preprint. Discussion started: 2 February 2026

- Small flux signals: Enhancements observed at Southern stations are only marginally larger than the model–data mismatch, limiting the inversion's ability to attribute them to specific sources. By contrast, larger enhancements at VND and CHI allow for clearer source identification.
- Geographical placement: Most Southern sites are not centrally located, reducing overlap between their footprints and the Italian landmass. POT is an exception, providing stronger coverage thanks to its central position.
- Meteorological conditions: Prevailing winds in the region do not consistently transport emissions from inland areas toward the stations, restricting their effectiveness in detecting key sources.

The TUR results (see Fig. C1) are consistent with these findings. CHI and VND yield identical, and the largest, uncertainty reductions, exceeding those of other sites by approximately 4%. VND has the strongest influence in Northern Italy, whereas CHI provides greater benefits in the rest of the country. Overall, TUR reaches 53% when all candidate stations are included (Scenario 11), and about 60% for the idealized network (Scenario 12).

These results underscore the importance of the CHI and VND sites for constraining CH_4 emissions in Italy, identifying them as the strongest candidates for extending the ICOS network in the country. Behind CHI and VND, ECO and CGR are also good candidates.

3.2 Sensitivity to truth

Figure 5 shows MER for all truths, emphasizing the large variability of results one can infer using different truth scenarios. Over the whole country, the MER is found to vary by up to 5% around the mean, which is large compared to the differences between scenario results. The truth has such an importance because the posterior scaling factors typically remain unchanged compared to the prior (i.e., close to 1) over areas where there are no monitoring stations, because of a lack of information. If the true scaling factors are also close to 1 over these areas, the agreement will appear to be large not because of constraints provided by the network, but because of randomness. For example, MER in the fourth truth scenario is notably low in Central Italy compared to the other scenarios. This arises because the fourth scenario includes a patch of high (randomly generated) scaling factors over this region. Due to the lack of observational constraints, the system cannot capture these values, and the posterior scaling factors remain close to 1, leading to a small MER. By contrast, in the other truth scenarios, some grid cells have true scaling factors already close to 1 in Central Italy. In these cases, even if the posterior values also stay near 1, the artificial agreement between the truth and posterior estimates leads to a larger MER. These results highlight that a robust assessment can only be achieved by using an ensemble of truth scenarios that captures the spread of emission uncertainties.

On the contrary, results for TUR are not dependent on truth scenarios. This is because the posterior error covariance matrix in Eq. 4 is a function only of the error covariance matrices (i.e., the prescribed prior relative uncertainties, correlation lengths, and model-data mismatch) and the transport model (see Thanwerdas et al. (2025) and references therein).

Because different truth realizations can yield different MER outcomes, it is important to assess how often one station provides stronger constraints than another, i.e., the probability that adding one station improves MER more than adding a different station. Figure 6 presents these pairwise comparisons. At the national scale, adding CHI outperforms VND in terms of MER

https://doi.org/10.5194/egusphere-2025-5804
Preprint. Discussion started: 2 February 2026

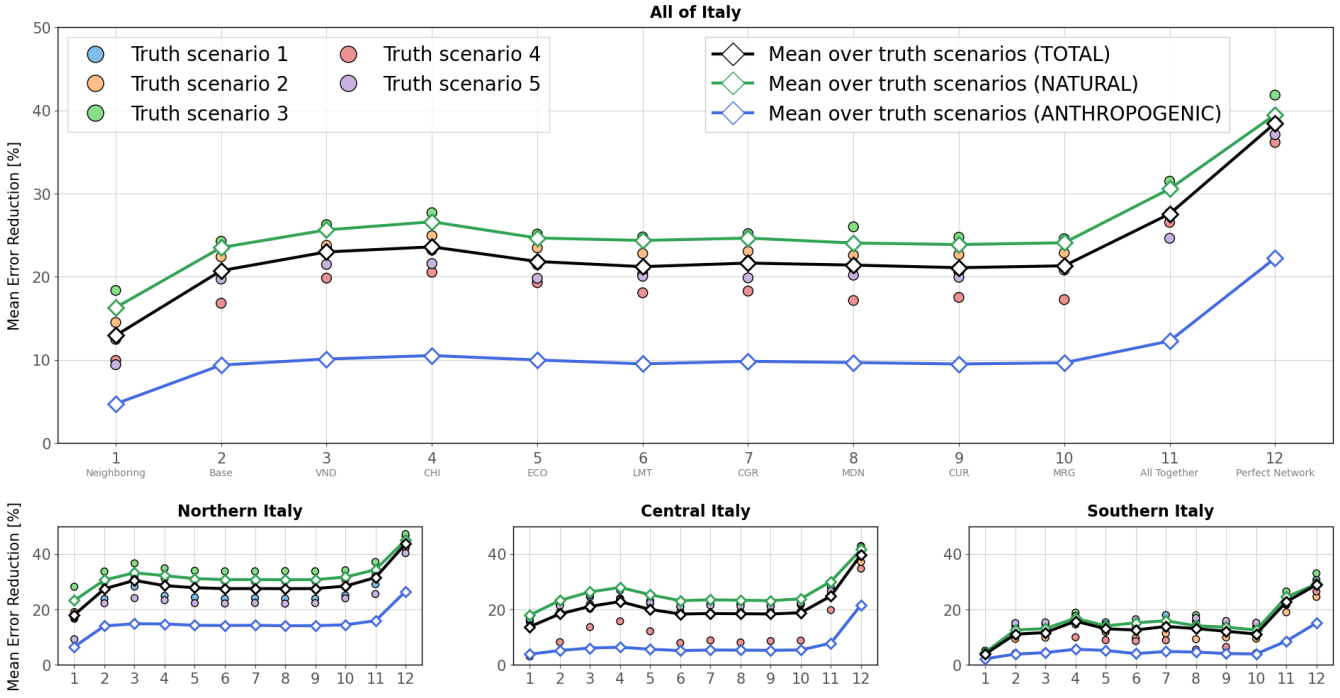

Figure 5. MER for each network scenario across Italy, as well as for Northern, Central, and Southern Italy. Black lines indicate MER for total emissions (averaged over all truth scenarios). Colored circles represent MER for total emissions under individual truth scenarios. Green and blue lines correspond to MER for natural and anthropogenic emissions, respectively.

for 80% of the truth realizations. This highlights the importance of using different truth scenarios. Using only one scenario could have resulted in preferring VND over CHI. In Northern Italy, VND consistently provides stronger constraints than CHI (100% of the realizations) as well as any other station. In Central Italy, CHI almost always outperforms VND, while VND tends to be better than the remaining stations. In Southern Italy, CHI is consistently superior to both VND and the other stations. However, while averages over the truth scenarios suggest that ECO, LMT, and CGR generally outperform VND in the South, a notable fraction of the realizations (20–40%) indicate better performance for VND. This highlights that, in some cases, VND can also provide stronger constraints than the Southern stations.

These results confirm that CHI and VND would be the best choices to extend the ICOS network in Italy. In addition, it shows slightly stronger results in favor of CHI, although the difference is small.

3.3 Anthropogenic and natural emissions

Distinguishing between the natural and anthropogenic components of the signal detected by a site is inherently challenging. In the absence of additional constraints, such as isotopes, only spatial and temporal differences between the two emission cate-

https://doi.org/10.5194/egusphere-2025-5804
Preprint. Discussion started: 2 February 2026

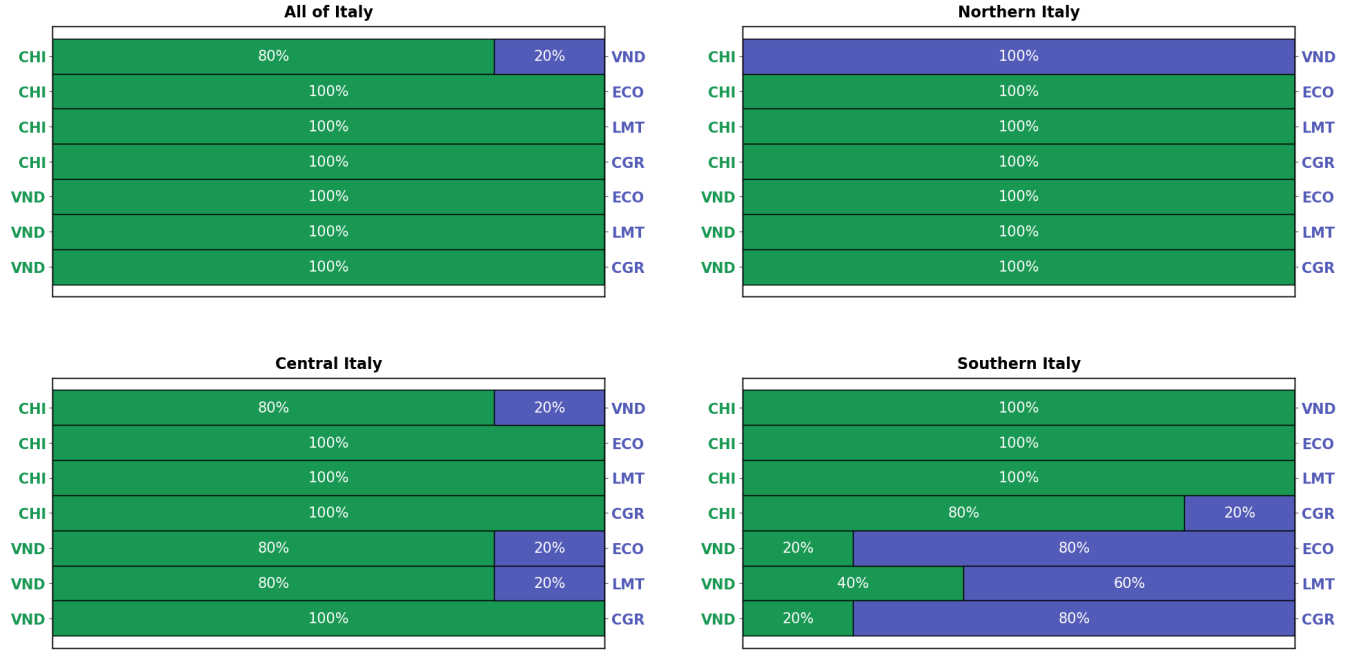

Figure 6. Pairwise comparison between network scenarios. In each comparison, the horizontal bar is divided into two sub-bars (green and blue). The green sub-bar (and its associated percentage) represents the fraction of truth scenarios in which adding the first station (green) yields a greater improvement in MER than adding the second station (blue). Conversely, the blue sub-bar (and its percentage) indicates the fraction of truth scenarios where adding the second station (blue) leads to a larger MER improvement than the first. For example, CHI outperforms VND in terms of MER for all of Italy in 80% of the truth scenarios.

gories can be exploited. When natural and anthropogenic emissions are co-located and occur simultaneously, the optimization process cannot effectively separate them, resulting in poor agreement between the posterior and true fluxes.

Figure 5 and Fig. C2 show MER and TUR results for total, anthropogenic and natural emissions, across all network scenarios. At the national scale, MER and TUR for anthropogenic emissions reach approximately 10% and 15-20%, respectively, across all candidate stations. These emissions are best constrained in Northern Italy, where they are most prevalent: adding VND (network scenario 3) yields a MER of 15% and a TUR close to 20%, the strongest performance in this region. In contrast, anthropogenic emissions remain poorly constrained in Central and Southern Italy, with both MER and TUR below 10%. Outcomes for natural emissions closely mirror those for total emissions, with MER values roughly 4% higher in all regions except the South, where they are nearly identical. Importantly, MER and TUR for total emissions are not simple weighted averages of their anthropogenic and natural counterparts. Because these metrics involve ratios, squared sums, and absolute sums, non-linear effects arise that prevent straightforward aggregation.

Natural emissions are more accurately captured than anthropogenic emissions, for the mean over truth scenarios (see Fig. 5 for MER and Fig 7 for TUR) and across all truth scenarios (not shown here). This is primarily due to differences in the prescribed correlation lengths used to define error statistics and construct the prior error-covariance matrix. A longer correlation

https://doi.org/10.5194/egusphere-2025-5804
Preprint. Discussion started: 2 February 2026

length reduces the degrees of freedom in the inverse problem and simplifies it. In other words, the true scaling factors for natural emissions vary less spatially than those for anthropogenic emissions. As a result, representing the higher spatial variability of anthropogenic scaling factors with the same number of observations is more challenging, leading to poorer performance. Unlike anthropogenic emissions, natural emissions are also more spatially diffuse in all regions. For this reason and because of the longer correlation lengths, optimizing natural emissions does not rely as heavily on ideal wind conditions (i.e., winds blowing predominantly from the region of interest toward the station).

Across all regions, the conclusions for anthropogenic and natural emissions mirror those for total emissions: CHI and VND outperform the other sites, with VND showing better performance in Northern Italy and CHI in the other regions.

3.4 Seasonality

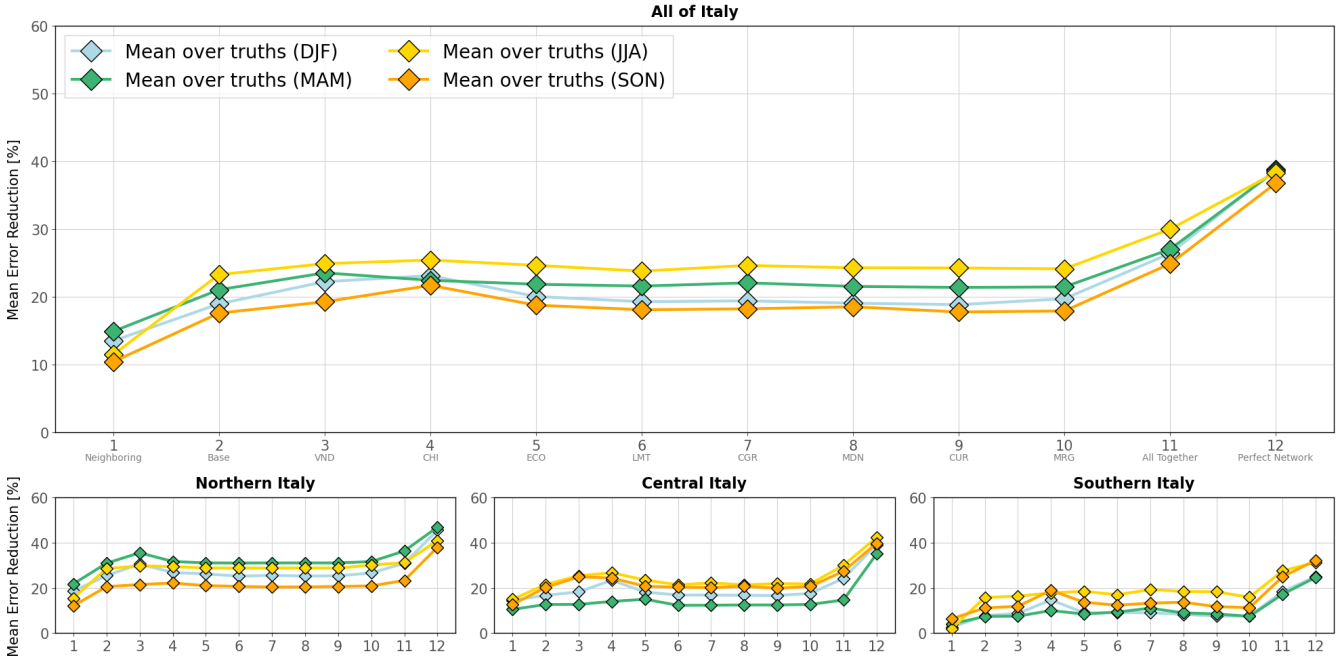

Figure 7. MER for each scenario over all of Italy, Northern Italy, Central Italy, and Southern Italy. Blue, green, yellow and orange lines represent MER for total emissions (mean over truth scenarios) in DJF (December-January-February), MAM (March-April-May), JJA (June-July-August) and SON (September-October-November), respectively.

Different scaling factors were generated for each season to account for temporal variability in the uncertainties. As a result, randomness could, in principle, overly influence the outcomes (only for MER as explained in Sect. 3.2) and limit the robustness of direct comparisons. However, in our case, the results remain consistent whether averaging over three, four or five truth scenarios. This suggests that randomness does not substantially affect the comparison, and that the conclusions drawn below are robust and informative.

https://doi.org/10.5194/egusphere-2025-5804
Preprint. Discussion started: 2 February 2026

Seasonality can have a substantial influence on MER mainly through two drivers:

- Larger flux signals: As mentioned in Sect 3.1, if enhancements become significantly larger than the model-data mismatch, the inversion system can better identify and locate the sources responsible for these enhancements. While natural emissions, particularly wetlands, are larger in summer because of rising temperature and daylight, anthropogenic emissions are larger in winter because of a higher demand for residential and industrial heating.
- Meteorological conditions: Seasonal shifts in prevailing winds and turbulent mixing can influence how emissions are transported from source regions to stations, and therefore affect the results.

For most of network scenarios, the best MER results for total emissions are obtained in JJA across all of Italy, including Central and Southern regions. Results for natural emissions closely mirror this pattern, indicating that the stronger signals from natural emissions in JJA are a key driver of the higher MER. However, this cannot be the sole explanation: although natural emissions are larger in MAM than in SON or DJF, the MER reaches its lowest values in MAM for Central Italy and remains very low in Southern Italy, while it peaks in JJA. This discrepancy is explained by wind patterns. In MAM 2018, winds in Central and Southern Italy were strong and predominantly from the West, limiting the transport of inland emissions toward the observation sites. By contrast, in JJA the winds were mostly from the North-West, allowing stations to sample more inland emissions and thereby improving the MER. Northern Italy shows a different situation: winds blow both from the East and the West throughout the year, with a higher frequency of easterly winds. The direction does not have a strong seasonal dependence but the speed is smaller in JJA, resulting in a complex interaction between emission intensity and wind speed to determine in which season MER is larger in Northern Italy. Unlike total and natural emissions, results for anthropogenic emissions (Fig. C4) are not substantially influenced by seasonality ($\pm$ 2%). There is only a slight advantage for SON and DJF, consistent with the anthropogenic emissions being larger in these seasons.

TUR does not depend on truth scenarios, so randomness does not influence the results. The outcomes generally mirror those of MER, with one notable exception: results in SON are substantially better compared to the other seasons. This improvement is likely due to winds in Southern and Central Italy during 2018 blowing from multiple directions, which broadened the footprints. Although such mixing does not improve MER since the signal becomes less distinguishable, it can reduce uncertainty across a wider area, thereby enhancing TUR. For anthropogenic emissions (Fig. C5), best results are obtained in DJF and in Northern Italy, because both the winds and the emissions are higher during this season.

Although seasonality affects both MER and TUR for individual network scenarios, the differences between scenarios show little seasonal variation; in other words, the seasonal influence is largely similar across all stations. Only VND and CHI show a marked performance increase in DJF, particularly in Northern and Central Italy. This improvement arises from their ability to better constrain anthropogenic emissions, which peak during this season.

https://doi.org/10.5194/egusphere-2025-5804
Preprint. Discussion started: 2 February 2026

3.5 Sensitivity to model-data mismatch

We evaluate the impact of incorporating a non-uniform model–data mismatch in our analysis. For real stations, this mismatch is estimated using observations from the AVENGERS obspack data product. For candidate stations, where observations are unavailable, we rely solely on simulated values.

For the real stations, we first perform a forward simulation for the year 2018. Simulated values are then sampled and compared to observations to compute an initial model–data mismatch using the root mean square error (RMSE). This initial estimate is used to perform an inversion for 2018. Following the inversion, we recalculate the RMSE, which serves as a refined estimate of the model–data mismatch for these stations.

For the candidate stations, a forward simulation for 2018 is also conducted. In this case, we use the standard deviation of the simulated values at each station as a proxy for model–data mismatch. This approach was validated against real stations, showing a strong correlation with the RMSE-based estimates (r = 0.96). We also tested alternative methods based on a moving average (7-day and monthly) of the simulated values, following Villalobos et al. (2025), but found that it yielded weaker correlations. Such differences might be related to the fact that CO_2 concentrations often show strong hourly fluctuations driven by the diurnal cycle of photosynthesis and respiration, unlike CH_4. Therefore, a 7-day moving average may be suitable for CO_2 but less representative for CH_4.

Results obtained using the non-uniform model–data mismatch are provided in the Supplementary Information. Most inferred mismatches exceed 20 ppb (Table S1), with a mean value of 31 ppb, indicating lower confidence in the measurements than initially expected. As a result, both MER (Table S2 and Figure S2) and TUR (Table S3 and Figure S3) decrease by 2–6% compared to the experiments assuming a uniform model–data mismatch. JFJ exhibits the smallest mismatch (14 ppb), whereas IPR and IT-BFt show the largest values (75 ppb). Large model–data mismatches suggest difficulties in capturing the observed variability at these stations. In particular, observations at IPR are known to be challenging for transport models due to the complex surrounding terrain. The CHI model–data mismatch (46 ppb) is estimated to be larger than that of VND (35 ppb), giving a slight advantage to VND compared to the experiments with a uniform mismatch. Nevertheless, the conclusions drawn in the previous sections remain unchanged: CHI and VND continue to be the optimal choices, with CHI retaining only a marginal advantage.

4 Discussion

In this study, we conducted an extensive analysis of network scenarios in Italy using OSSEs and inverse modelling. One of the main added values of this work is the creation of multiple truth scenarios, which limits the influence of randomness. Nonetheless, our methodology also entails several caveats and limitations. Most of these could be addressed with additional simulations, but this would significantly increase the computational cost of the analysis.

A first limitation lies in the assumption of perfect knowledge of prior relative uncertainties and correlation lengths in the inversion setup. In reality, these parameters can only be approximated. Introducing a mismatch between the assumed values and those used to generate the true scaling factors would have affected the optimal solution and reduced performance (Steiner

https://doi.org/10.5194/egusphere-2025-5804
Preprint. Discussion started: 2 February 2026

et al., 2024a). However, we expect this reduction would have occurred uniformly across network scenarios, leaving the main conclusions regarding VND and CHI unchanged.

Similarly, the model–data mismatch applied to perturb the synthetic observations was prescribed to follow a normal distribution, which may not hold for real data. Deviations from this assumption could further degrade inversion performance. It is therefore important to understand that these results are produced with perfect knowledge.

We performed the OSSEs for the year 2018 to ensure consistency with Villalobos et al. (2025). Although dominant winds generally remain stable from year to year at the national scale, local variations can occur that may alter the emission signals captured by the stations and, consequently, the results. A more comprehensive picture would require reproducing this study over multiple years. However, the computational demands of such an analysis remain a major limitation and make it difficult to implement in practice.

We assumed an inlet height of 100 m for most lowland candidate stations, implying the construction of tall towers at these sites on top of existing infrastructure. This sampling height was chosen to maximize station performance and to ensure comparability across network scenarios involving lowland sites. Our results should therefore be interpreted with this assumption in mind. Although they suggest that extending the network by adding CHI is the best option, sampling concentrations at CHI with the current inlet height (15 m) rather than 100 m may not be appropriate and could lead to poorer performance compared with extending the network with VND, which would not require additional infrastructure.

Although in principle this Eulerian-model-based methodology could be extended to determine the optimal location of a measurement station over the whole domain, such an application would require as many inversions as grid cells in the model domain, and considerably more if multiple sampling heights and truth scenarios were also tested. At present, this is computationally infeasible, and analyses must remain restricted to a manageable set of candidate stations. Notably, the inclusion of multiple truth scenarios already demanded significantly greater computational resources than are typically required for OSSEs.

In this case study, which involves only surface stations, using an Eulerian model offers no clear advantages compared to using a Lagrangian model. It is computationally more demanding, as the model must be rerun for each inversion. In contrast, a Lagrangian model requires the computation of footprints only once, which can then be reused to perform multiple inversions efficiently. Furthermore, the same evaluation metrics can be derived just as easily within a Lagrangian framework. However, the computational cost of Lagrangian modeling scales with the number of observations. When assimilating satellite data, this number can become extremely large, making Lagrangian approaches computationally prohibitive. Conversely, the Eulerian-based methodology introduced here can be directly applied to a massive set of observations produced by satellites without additional computational burden.

We employed two complementary evaluation metrics: the TUR and the MER. While these two metrics are highly correlated (experiments with a high TUR often exhibit a high MER and vice versa), the correlation is not perfect, as shown in Figure S4 in the Supplementary Information. For instance, SON and MAM yield similar TUR values for total emissions in Northern Italy, yet their MER can differ by as much as 10% (see Table B1 and Table B2), which is substantial. In our experiments, such decorrelation between the two metrics occurs mainly when seasonal dependence is introduced. When it is removed, the correlation between TUR and MER becomes much stronger. As discussed earlier, variable wind conditions can improve spatial coverage

https://doi.org/10.5194/egusphere-2025-5804
Preprint. Discussion started: 2 February 2026

around the station, leading to a high TUR. However, this same variability can make it harder to localize the signal accurately, resulting in a low MER. Thus, a trade-off exists between TUR and MER, underscoring the importance of considering both metrics when evaluating network performance. In practical, real-data applications, MER cannot be computed because the true emission values are unknown. Although TUR generally provides a reasonable proxy for assessing the agreement between posterior and true emissions, low posterior uncertainties do not necessarily imply that the mean posterior estimates are accurate. This emphasizes the importance of reporting the full range of plausible estimates rather than central estimates only.

Villalobos et al. (2025) conducted a similar study focusing on CO_2 rather than CH_4, using a Lagrangian-based framework. The candidate stations were identical, with the same inlet heights. Although they did not use the same evaluation metrics, they both quantified the uncertainty reduction and the agreement between posterior and true CO_2 fluxes, using a single truth scenario. Despite using inversion setups different from ours, they also found that CHI provides the strongest constraint among the candidate stations, with VND being the second-best site in terms of uncertainty reduction. When two stations were added to the network, the CHI–ECO combination yielded the best performance. This result is somewhat counterintuitive, as adding ECO alone provided weaker constraints, both in terms of agreement with true fluxes and uncertainty reduction, than CUR or MRG, consistent with our findings. This suggests that station synergies cannot be simply inferred from the sum of individual station impacts. Although we could not test multi-station combinations due to computational limitations, the strong agreement between our single-station results and those of Villalobos et al. (2025) indicates that the overall outcome would likely be similar. These findings reinforce that CHI is the most promising candidate for expanding the Italian observation network. CHI appears to be strategically located to capture key transport patterns and flux signals influencing both gases, highlighting its importance as a potential addition to the ICOS network. From a policy perspective, establishing CHI as a multi-species observation site could provide more robust data to support national greenhouse gas reporting and independent verification under international climate frameworks.

Finally, it is important to note that, except for scenarios 11 and 12, which feature multiple stations, differences in results between network scenarios are small, indicating that no single station can significantly improve coverage in Italy. Although CHI and VND perform slightly better individually, it is only when multiple stations are strategically placed that the network can effectively constrain fluxes.

5 Conclusions

In this study, we conducted Observing System Simulation Experiments (OSSEs) to assess the potential expansion of the ICOS monitoring network in Italy for CH_4. This work complements the recent study by Villalobos et al. (2025), which focused on CO_2. Our results show that CHI and VND are the most promising candidate stations for improving emission constraints in Italy, with CHI having a slight advantage when sampling at 100 m. While CHI provides stronger constraints in Central and Southern Italy, VND is particularly effective in Northern Italy.

https://doi.org/10.5194/egusphere-2025-5804
Preprint. Discussion started: 2 February 2026

To evaluate the impact of adding these stations, we introduced two complementary metrics: the mean error reduction (MER) and the total flux uncertainty reduction (TUR). These metrics were applied to estimate the effect of new stations on total, anthropogenic, and natural emissions, both annually and seasonally, for three Italian regions as well as the entire country.

We also tested multiple truth scenarios to account for randomness in generating both true emissions and synthetic observations. The analysis shows that randomness strongly influences the results, highlighting the limitations of relying on a single truth scenario. In addition, we quantified the effect of assuming a non-uniform model–data mismatch and found that, in this case study, it did not significantly alter the results.

The methodology we present can be readily applied to other Eulerian models and adapted to different countries or regions. While computationally demanding, this type of OSSE study offers valuable guidance for decision-makers and atmospheric scientists when selecting candidate sites and optimizing observational coverage.

Code and data availability. The ICON and ART codes are open source and publicly available for download at https://doi.org/10.35089/WDCC/IconRelease01 (ICON Partnership, 2024). The CIF code featuring the new EnSRF mode can be accessed via the following DOI: https://doi.org/10.5281/zenodo.12742377 (Berchet et al., 2022). Complete and surface ERA5 reanalysis data are publicly available via the Copernicus Climate Change Service at https://doi.org/10.24381/cds.143582cf (Hersbach et al., 2017) and https://doi.org/10.24381/cds.adbb2d47 (Hersbach et al., 2023), respectively.

Author contributions. JT and DB designed the experiments. JT performed the simulations and led the manuscript preparation. PC provided valuable information about the Italian observation network. RD, SVM and AF created the TNO-AVENGERS emission inventory. ZW performed the LPJ-GUESS runs. YV contributed her scientific expertise. All co-authors reviewed the manuscript and contributed to the writing with corrections and comments.

Competing interests. The authors declare they have no competing interests.

Acknowledgements. This project has received funding from the European Union's Horizon Europe programme under grant agreement no. 101081322 (AVENGERS). The CIF-ICON-ART inversions were conducted at the Swiss National Supercomputing Centre (CSCS) under grant No. sm104 and were supported by the Center for Climate Systems Modeling (C2SM). The Italian ICOS stations received funding from the Italian Ministry of University and Research (MUR) under the Joint Research Unit "ICOS-Italy", the project PRO-ICOS MED (CUP B27E19000040007), funded by the European Regional Development Fund and co-funded by the National Cohesion Fund (FSC) and the Project IR0000032 – ITINERIS (CUP B53C22002150006) funded by EU - Next Generation EU PNRR.

https://doi.org/10.5194/egusphere-2025-5804
Preprint. Discussion started: 2 February 2026

Appendix A: Surface stations

Table A1. List of candidate stations. The inlet height provided here represents a preliminary estimate for a potential ICOS station that could operate at this location.

ID	Name	Country	Latitude	Longitude	Altitude (m.a.s.l.)	Inlet height (m.a.g.l.)
CGR	Capo Granitola	IT	37.57	12.66	10	2
CHI	Chieti	IT	42.18	14.69	3	50
CUR	Monte Curcio	IT	39.32	16.42	1796	2
ECO	Lecce	IT	40.34	18.12	36	100
LMT	Lamezia Terme	IT	38.88	16.23	6	100
MDN	Madonia - Piano Battaglia	IT	37.88	14.03	1650	2
MRG	Col Margherita	IT	46.37	11.80	2543	2
VND	Mount Venda	IT	45.31	11.68	600	100

https://doi.org/10.5194/egusphere-2025-5804
Preprint. Discussion started: 2 February 2026

Table A2. List of existing ICOS atmosphere surface stations in Italy and in the surrounding countries.

ID	Name	Country	Latitude	Longitude	Altitude (m.a.s.l.)	Inlet height (m.a.g.l.)
BRM	Beromünster	CH	47.19	8.18	797	212
CMN	Monte Cimone	IT	44.19	10.70	2165	8
ERS	Ersa	FR	42.97	9.38	533	40
HEI	Heidelberg	DE	49.42	8.68	113	30
HPB	Hohenpeissenberg	DE	47.80	11.02	934	131
HUN	Hegyhátsál	HU	46.96	16.65	248	115
IPR	Ispra	IT	45.81	8.64	210	100
JFJ	Jungfraujoch	CH	46.55	7.99	3572	14
KAS	Kasprowy Wierch	PL	49.23	19.98	1987	7
KIT	Karlsruhe	DE	49.09	8.42	110	200
KRE	Křešín u Pacova	CZ	49.57	15.08	534	250
LHW	Laegern-Hochwacht	CH	47.48	8.40	840	32
LMP	Lampedusa	IT	35.52	12.63	45	8
OHP	Observatoire de Haute Provence	FR	43.93	5.71	650	100
OPE	Observatoire pérenne de l'environnement	FR	48.56	5.50	390	120
PRS	Plateau Rosa	IT	45.94	7.71	3480	10
POT	Potenza	IT	40.60	15.72	760	100
SSL	Schauinsland	DE	47.90	7.92	1205	6
ZSF	Zugspitze	DE	47.42	10.98	2666	3

https://doi.org/10.5194/egusphere-2025-5804
Preprint. Discussion started: 2 February 2026

Table A3. List of ICOS ecosystem surface stations. The inlet height provided here represents a preliminary estimate for a potential ICOS station that could operate at this location.

ID	Name	Country	Latitude	Longitude	Altitude (m.a.s.l.)	Fake inlet height (m.a.g.l.)
IT-BCi	Borgo Cioffi	IT	40.52	14.96	15	100
IT-BFt	Bosco Fontana	IT	45.20	10.74	37	100
IT-Col	Collelongo	IT	41.82	13.59	1560	2
IT-Cp2	Castelporziano2	IT	41.70	12.36	13	100
IT-Lpd	Lampedusa Ecosystem Observatory	IT	35.53	12.54	45	100
IT-Lsn	Lison	IT	45.74	12.75	1	100
IT-MBo	Monte Bondone	IT	46.01	11.05	1550	2
IT-Niv	Nivolet	IT	45.49	7.14	2708	2
IT-Noe	Arca di Noe - Le Prigionette	IT	40.61	8.15	25	100
IT-Oxm	Osservatorio Ximeniano Firenze	IT	43.77	11.26	50	100
IT-PCm	Parco Urbano di Capodimonte	IT	40.87	14.25	148	100
IT-Ren	Renon	IT	46.59	11.43	1735	2
IT-Sas	Sassari	IT	40.84	8.40	25	100
IT-SR2	San Rossore 2	IT	43.73	10.29	4	100
IT-Tor	Torgnon	IT	45.84	7.58	2168	2
IT-TrF	Torgnon-LD	IT	45.82	7.56	2091	2

https://doi.org/10.5194/egusphere-2025-5804
Preprint. Discussion started: 2 February 2026

Appendix B: MER and TUR values

Table B1. MER values for all network scenarios, regions, emission categories and seasons.

		SCENARIO	1	2	3	4	5	6	7	8	9	10	11	12
REGION	CATEGORY	SEASON												
ALL OF ITALY	TOTAL	FULL YEAR	13	21	23	24	22	21	22	21	21	21	28	38
		DJF	14	19	22	23	20	19	19	19	19	20	26	39
		MAM	15	21	24	22	22	22	22	22	21	21	27	39
		JJA	11	23	25	25	25	24	25	24	24	24	30	38
		SON	10	18	19	22	19	18	18	19	18	18	25	37
	NATURAL	FULL YEAR	16	24	26	27	25	24	25	24	24	24	31	39
		DJF	17	21	25	24	22	22	21	21	21	22	27	37
		MAM	17	23	26	24	24	23	24	23	23	23	30	40
		JJA	14	27	28	30	29	29	29	28	29	28	35	41
		SON	14	18	20	24	19	19	19	19	18	19	26	36
	ANTHROPOGENIC	FULL YEAR	5	9	10	11	10	10	10	10	10	10	12	22
		DJF	5	9	10	11	10	9	10	9	9	9	13	24
		MAM	5	9	11	10	10	10	10	10	10	10	12	21
		JJA	4	8	9	9	9	8	9	9	9	9	11	20
		SON	5	10	10	12	11	10	11	11	10	10	14	24
NORTHERN ITALY	TOTAL	FULL YEAR	18	27	30	29	28	27	28	27	28	28	31	44
		DJF	19	25	31	27	26	25	26	25	25	27	31	46
		MAM	22	31	36	32	31	31	31	31	31	32	36	47
		JJA	16	29	30	29	29	29	29	29	29	30	31	41
		SON	12	21	21	22	21	21	20	20	21	21	23	38
	NATURAL	FULL YEAR	23	31	33	32	31	31	31	31	31	32	34	45
		DJF	23	28	34	30	29	27	28	27	27	29	34	48
		MAM	25	34	40	36	34	34	35	34	34	35	41	50
		JJA	18	31	29	32	31	31	31	31	31	33	32	40
		SON	19	22	21	23	22	22	21	22	22	22	23	35
	ANTHROPOGENIC	FULL YEAR	7	14	15	15	14	14	14	14	14	14	16	26
		DJF	7	14	15	15	14	14	14	14	14	14	16	28
		MAM	8	14	16	14	14	14	14	14	14	15	16	27
		JJA	5	13	13	13	13	13	13	13	13	13	14	23
		SON	6	15	15	17	15	15	15	15	15	15	17	27
CENTRAL ITALY	TOTAL	FULL YEAR	14	18	21	23	20	18	19	18	18	19	25	40
		DJF	14	17	18	23	18	17	17	17	17	18	24	39
		MAM	11	13	13	14	15	12	12	12	12	13	15	35
		JJA	15	21	25	27	23	21	22	21	22	22	30	42
		SON	13	20	25	24	21	20	20	21	20	21	27	40
	NATURAL	FULL YEAR	18	23	26	28	25	23	23	23	23	24	30	42
		DJF	18	20	21	24	22	20	21	20	20	21	24	36
		MAM	14	16	15	17	19	16	15	16	16	16	17	36
		JJA	18	26	31	33	29	26	27	26	27	26	37	44
		SON	16	24	30	30	25	24	24	25	23	25	33	42
	ANTHROPOGENIC	FULL YEAR	4	5	6	6	6	5	5	5	5	5	8	22
		DJF	5	6	7	9	6	6	6	6	6	6	10	25
		MAM	4	5	6	6	6	5	6	5	5	5	7	18
		JJA	3	4	4	4	4	4	4	4	4	4	6	21
		SON	4	6	7	6	6	6	6	6	6	6	8	22
SOUTHERN ITALY	TOTAL	FULL YEAR	4	11	12	16	13	13	14	13	12	11	23	29
		DJF	3	8	9	15	9	9	9	8	8	8	18	25
		MAM	4	7	7	10	8	9	11	9	8	7	17	25
		JJA	2	16	16	18	18	17	19	18	18	16	28	31
		SON	6	11	12	19	14	12	13	14	12	11	25	32
	NATURAL	FULL YEAR	4	13	13	17	14	15	16	14	14	13	24	29
		DJF	3	9	10	13	9	12	9	9	8	9	16	19
		MAM	5	8	9	10	9	11	14	10	10	8	21	26
		JJA	2	20	21	22	22	23	24	22	22	20	33	36
		SON	8	8	9	19	9	10	10	9	8	8	24	31
	ANTHROPOGENIC	FULL YEAR	2	4	4	6	5	4	5	5	4	4	9	15
		DJF	2	4	5	6	5	4	5	4	4	4	9	16
		MAM	2	3	4	4	3	4	4	3	3	3	5	13
		JJA	2	3	4	5	5	3	4	4	4	3	8	13
		SON	3	5	5	7	7	5	6	6	5	5	12	18

https://doi.org/10.5194/egusphere-2025-5804
Preprint. Discussion started: 2 February 2026

Table B2. TUR values for all network scenarios, regions, emission categories and seasons.

		SCENARIO	1	2	3	4	5	6	7	8	9	10	11	12
REGION	CATEGORY	SEASON												
ALL OF ITALY	TOTAL	FULL YEAR	29	42	47	47	43	43	43	43	43	43	53	61
		DJF	24	35	44	39	36	36	35	35	35	35	49	58
		MAM	25	44	47	49	45	45	45	45	45	45	54	61
		JJA	33	44	49	48	44	45	45	44	45	45	55	62
		SON	32	45	47	49	46	46	46	45	45	45	53	63
	NATURAL	FULL YEAR	33	47	53	53	48	48	49	48	48	48	59	67
		DJF	31	41	51	46	42	42	42	42	42	41	56	65
		MAM	28	47	51	54	48	47	49	48	47	47	59	65
		JJA	37	49	54	54	49	50	50	50	50	50	60	68
		SON	35	50	54	55	51	52	52	51	51	51	60	69
	ANTHROPOGENIC	FULL YEAR	7	16	19	16	17	16	16	16	16	17	21	31
		DJF	8	23	26	23	24	23	23	23	23	23	28	38
		MAM	3	10	14	11	11	10	11	10	10	11	16	26
		JJA	6	15	18	15	15	15	15	15	15	15	21	29
		SON	10	16	18	16	17	16	16	16	16	17	19	32
NORTHERN ITALY	TOTAL	FULL YEAR	31	43	49	43	42	43	43	43	43	43	49	58
		DJF	27	37	48	38	37	37	37	37	37	37	49	58
		MAM	28	46	50	47	46	46	46	46	46	47	50	57
		JJA	33	42	49	43	42	42	42	42	42	43	50	58
		SON	34	43	45	43	43	43	43	43	43	44	46	58
	NATURAL	FULL YEAR	38	49	56	50	49	49	49	49	49	49	56	65
		DJF	36	44	56	45	44	44	44	44	44	44	57	65
		MAM	34	52	56	53	52	52	52	52	52	52	56	57
		JJA	41	50	56	50	49	50	50	50	50	50	55	61
		SON	41	49	52	49	48	49	49	49	49	50	53	64
	ANTHROPOGENIC	FULL YEAR	10	23	28	24	23	23	23	23	23	24	29	40
		DJF	12	31	37	32	32	32	32	32	31	32	38	48
		MAM	5	17	22	17	17	17	17	17	17	18	23	33
		JJA	10	21	27	22	21	21	21	21	21	22	29	38
		SON	12	23	27	23	23	23	23	23	23	24	27	38
CENTRAL ITALY	TOTAL	FULL YEAR	25	30	34	38	31	31	30	30	30	31	40	55
		DJF	20	22	27	28	23	23	22	22	22	22	32	49
		MAM	20	31	35	41	32	32	31	32	31	31	44	56
		JJA	30	33	36	39	33	33	33	33	33	34	42	56
		SON	29	33	35	39	34	34	33	33	33	33	41	57
	NATURAL	FULL YEAR	29	35	40	44	36	36	36	36	36	36	47	61
		DJF	27	30	35	37	30	30	30	30	30	30	41	58
		MAM	24	32	38	47	35	33	33	33	33	33	50	59
		JJA	32	37	39	43	37	37	37	37	37	37	46	61
		SON	33	39	43	45	40	40	39	39	39	40	48	63
	ANTHROPOGENIC	FULL YEAR	4	6	7	8	7	7	7	6	7	7	9	29
		DJF	5	7	8	8	7	7	7	7	7	7	9	26
		MAM	4	7	7	9	7	7	7	7	7	7	10	30
		JJA	3	4	4	5	5	4	4	4	4	4	6	24
		SON	5	8	8	9	9	9	8	8	8	9	10	34
SOUTHERN ITALY	TOTAL	FULL YEAR	5	30	31	38	33	34	34	33	32	30	47	50
		DJF	2	28	30	36	31	31	31	29	28	28	42	46
		MAM	3	26	27	32	28	29	31	30	29	26	43	47
		JJA	7	34	34	42	36	37	37	36	35	34	49	51
		SON	6	31	32	38	34	35	36	35	33	31	49	53
	NATURAL	FULL YEAR	6	35	36	44	37	39	40	38	37	35	54	57
		DJF	4	35	37	44	37	38	38	36	35	35	51	54
		MAM	4	23	24	29	26	27	30	27	26	23	46	49
		JJA	7	38	39	48	40	42	42	40	40	39	56	59
		SON	8	39	40	45	41	43	44	42	40	39	58	62
	ANTHROPOGENIC	FULL YEAR	2	4	4	4	6	4	5	5	4	4	9	14
		DJF	2	5	5	4	9	6	5	5	5	5	10	15
		MAM	1	3	3	4	4	3	5	5	3	3	9	16
		JJA	2	4	5	5	7	5	5	5	4	4	9	11
		SON	2	3	3	4	6	3	4	4	3	3	8	16

https://doi.org/10.5194/egusphere-2025-5804
Preprint. Discussion started: 2 February 2026

Appendix C: Additional figures

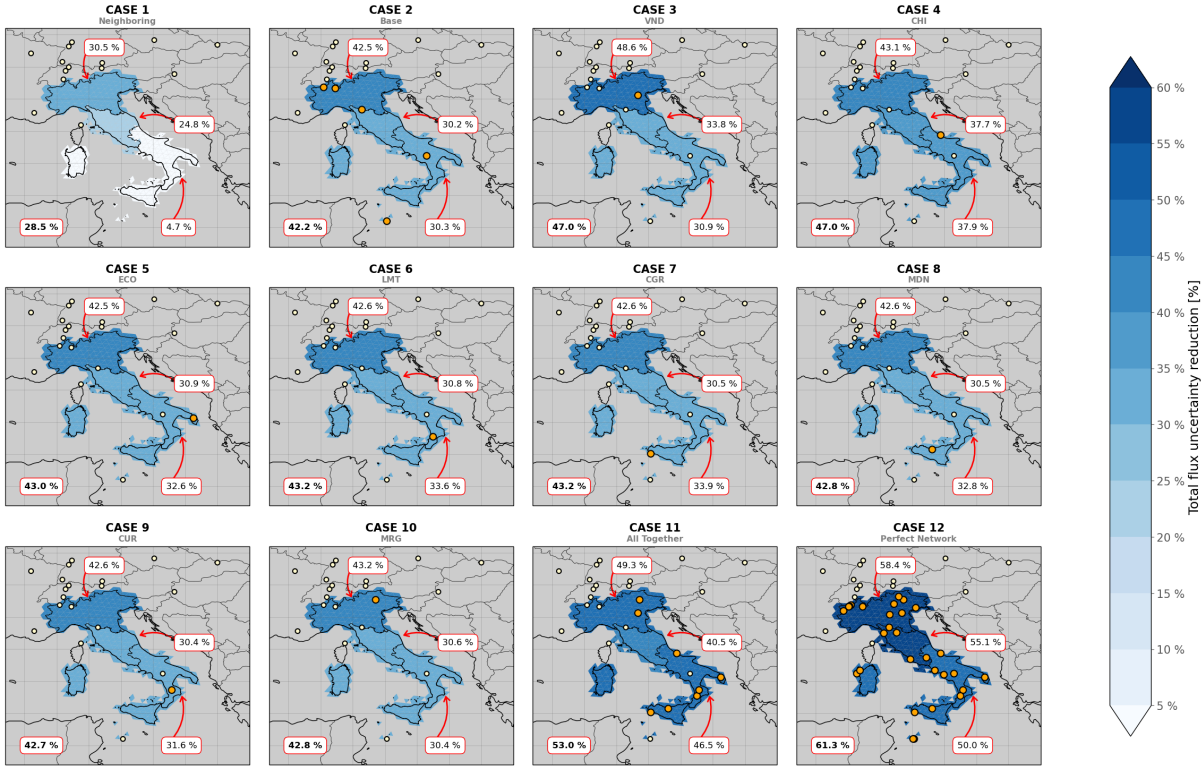

Figure C1. Spatial distribution of TUR across Italy, shown separately for the whole country, Northern Italy, Central Italy, and Southern Italy. For each region, the corresponding TUR value is annotated in a box placed near its location, while the national value is displayed in the lower-left corner of each panel, in bold. Stations from Scenario 1 are marked with yellow circles, and additional stations introduced in subsequent scenarios are shown as orange circles.

https://doi.org/10.5194/egusphere-2025-5804
Preprint. Discussion started: 2 February 2026

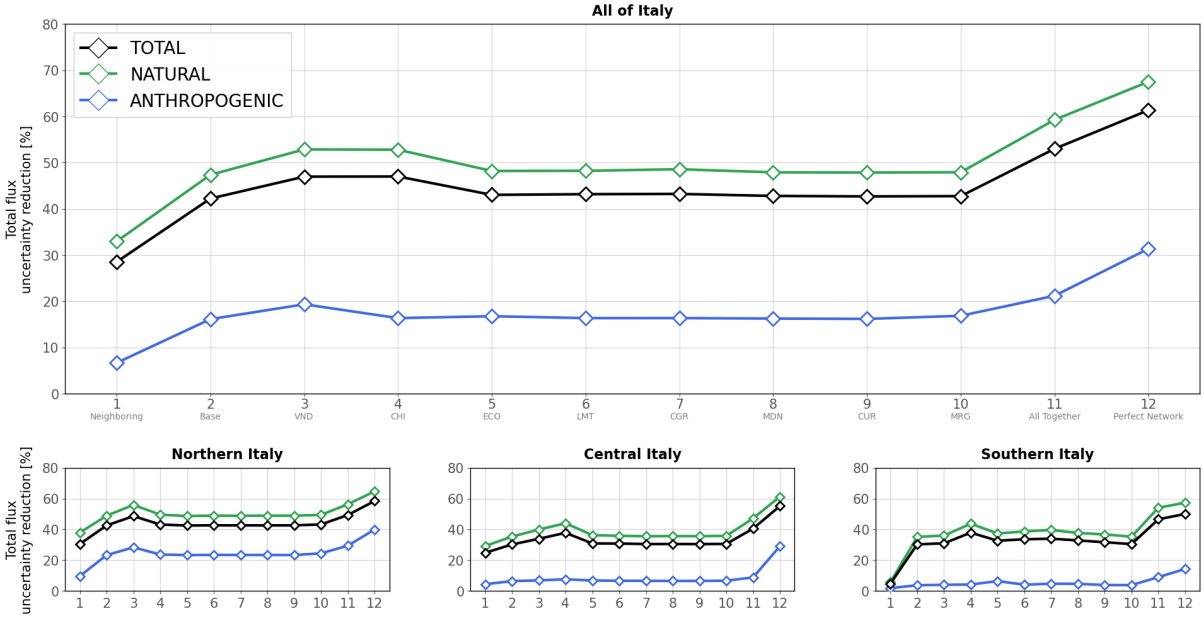

Figure C2. TUR for each network scenario across Italy, as well as for Northern, Central, and Southern Italy. Black lines indicate TUR for total emissions. Green and blue lines correspond to TUR for natural and anthropogenic emissions, respectively.

https://doi.org/10.5194/egusphere-2025-5804
Preprint. Discussion started: 2 February 2026

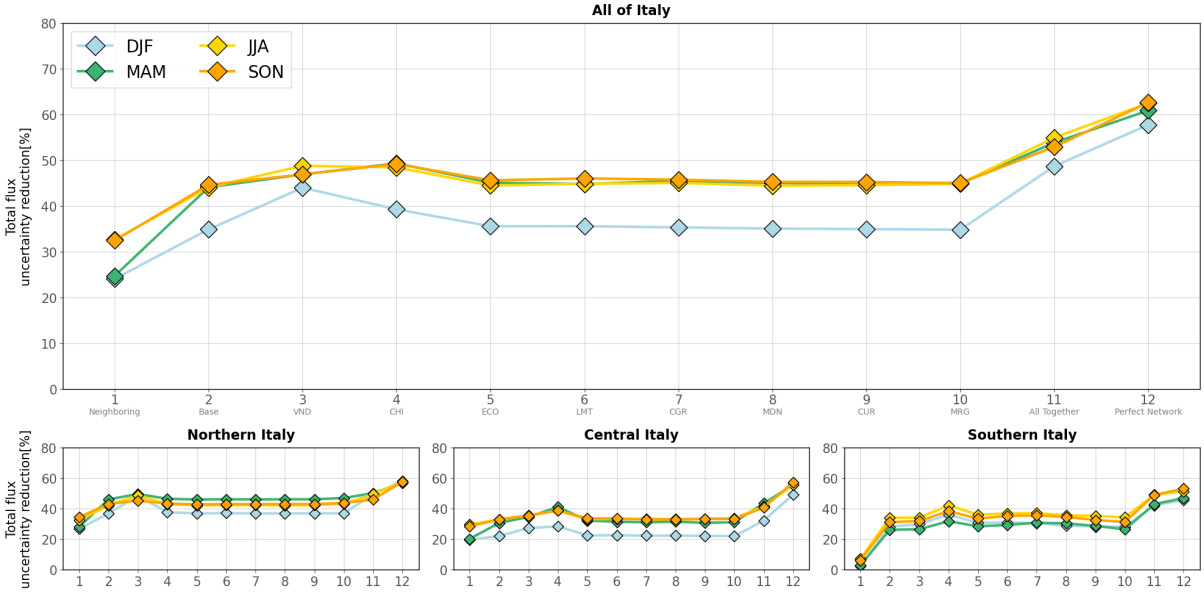

Figure C3. TUR for each scenario over all of Italy, Northern Italy, Central Italy, and Southern Italy. Blue, green, yellow and orange lines represent TUR for total emissions in DJF, MAM, JJA and SON, respectively.

https://doi.org/10.5194/egusphere-2025-5804
Preprint. Discussion started: 2 February 2026

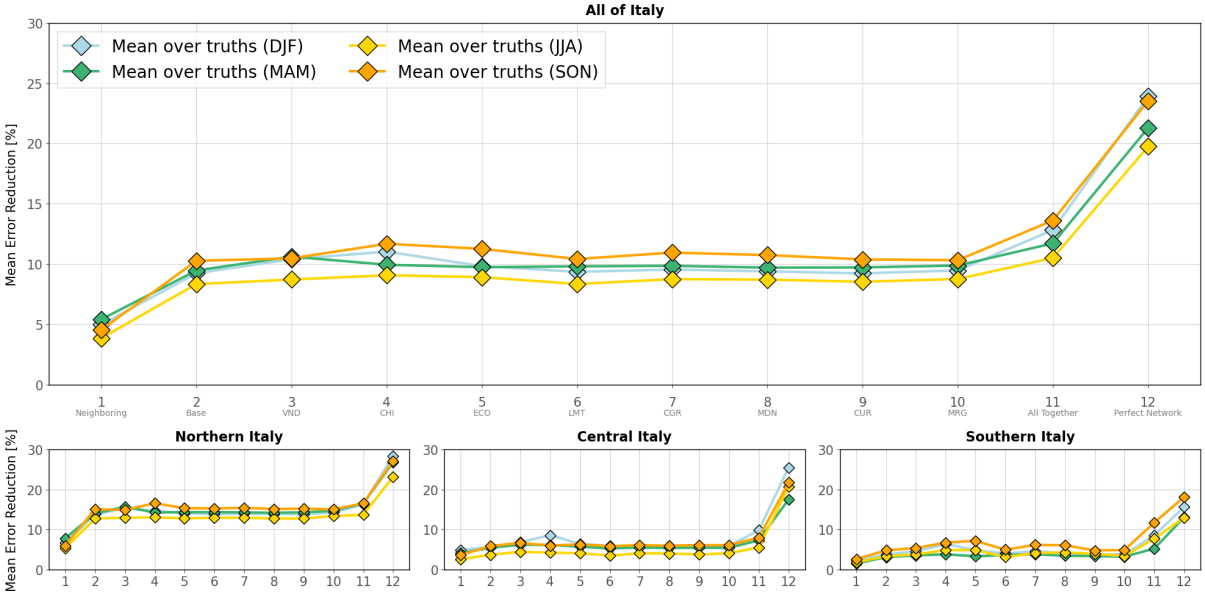

Figure C4. Same as Fig. 7, but for anthropogenic emissions.

https://doi.org/10.5194/egusphere-2025-5804
Preprint. Discussion started: 2 February 2026

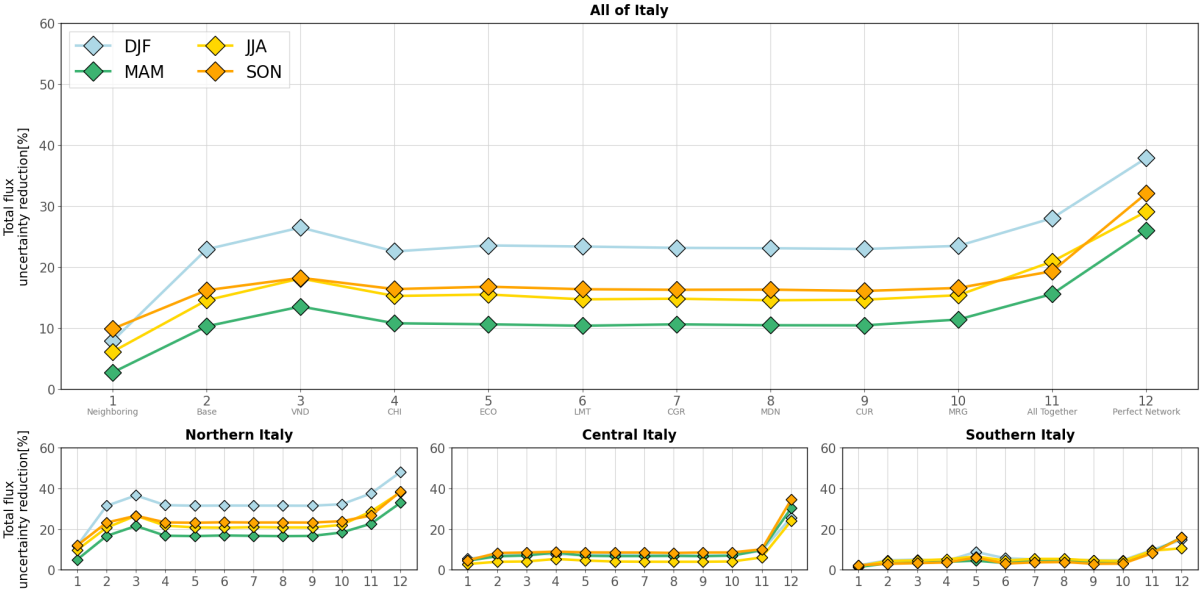

Figure C5. Same as Fig. C3, but for anthropogenic emissions.

https://doi.org/10.5194/egusphere-2025-5804
Preprint. Discussion started: 2 February 2026

References

Baker, D. F., Bösch, H., Doney, S. C., O'Brien, D., and Schimel, D. S.: Carbon Source/Sink Information Provided by Column CO_2 Measurements from the Orbiting Carbon Observatory, Atmospheric Chemistry and Physics, 10, 4145–4165, https://doi.org/10.5194/acp-10-4145-2010, 2010.

Basu, S., Miller, J. B., and Lehman, S.: Separation of Biospheric and Fossil Fuel Fluxes of CO_2 by Atmospheric Inversion of CO_2 and $^{14}CO_2$ Measurements: Observation System Simulations, Atmospheric Chemistry and Physics, 16, 5665–5683, https://doi.org/10.5194/acp-16-5665-2016, 2016.

Bencardino, M.: Atmospheric CH_4 at Monte Curcio by CNR-Institute of Atmospheric Pollution Research, https://doi.org/10.50849/WDCGG_0037-6056-1002-01-01-9999, dataset published as CH4_CUR6056_surface-insitu_IIA_data1, 2025.

Berchet, A., Sollum, E., Thompson, R. L., Pison, I., Thanwerdas, J., Broquet, G., Chevallier, F., Aalto, T., Berchet, A., Bergamaschi, P., Brunner, D., Engelen, R., Fortems-Cheiney, A., Gerbig, C., Groot Zwaaftink, C. D., Haussaire, J.-M., Henne, S., Houweling, S., Karstens, U., Kutsch, W. L., Luijkx, I. T., Monteil, G., Palmer, P. I., van Peet, J. C. A., Peters, W., Peylin, P., Potier, E., Rödenbeck, C., Saunois, M., Scholze, M., Tsuruta, A., and Zhao, Y.: The Community Inversion Framework v1.0: A Unified System for Atmospheric Inversion Studies, Geoscientific Model Development, 14, 5331–5354, https://doi.org/10.5194/gmd-14-5331-2021, 2021.

Berchet, A., Sollum, E., Pison, I., Thompson, R. L., Thanwerdas, J., Fortems-Cheiney, A., Peet, J. C. A. v., Potier, E., Chevallier, F., Broquet, G., and Berchet, A.: The Community Inversion Framework: codes and documentation, https://doi.org/10.5281/zenodo.6304912, 2022.

Bergamaschi, P., Danila, A., Weiss, R. F., Ciais, P., Thompson, R. L., Brunner, D., Levin, I., Meijer, Y., Chevallier, F., Janssens-Maenhout, G., Bovensmann, H., Crisp, D., Basu, S., Dlugokencky, E., Engelen, R., Gerbig, C., Günther, D., Hammer, S., Henne, S., Houweling, S., Karstens, U., Kort, E., Maione, M., Manning, A. J., Miller, J., Montzka, S., Pandey, S., Peters, W., Peylin, P., Pinty, B., Ramonet, M., Reimann, S., Röckmann, T., Schmidt, M., Strogies, M., Sussams, J., Tarasova, O., van Aardenne, J., Vermeulen, A. T., and Vogel, F.: Atmospheric Monitoring and Inverse Modelling for Verification of Greenhouse Gas Inventories,, LUX, ISBN 978-92-79-88939-4, https://doi.org/10.2760/02681, 2018.

Bloom, A. A., Lauvaux, T., Worden, J., Yadav, V., Duren, R., Sander, S. P., and Schimel, D. S.: What Are the Greenhouse Gas Observing System Requirements for Reducing Fundamental Biogeochemical Process Uncertainty? Amazon Wetland CH_4 Emissions as a Case Study, Atmospheric Chemistry and Physics, 16, 15 199–15 218, https://doi.org/10.5194/acp-16-15199-2016, 2016.

Calvo Buendia, E., Tanabe, K., Kranjc, A., Baasansuren, J., Fukuda, M., Ngarize, S., Osako, A., Pyrozhenko, Y., Shermanau, P., and Federici, S., eds.: 2019 Refinement to the 2006 IPCC Guidelines for National Greenhouse Gas Inventories, Intergovernmental Panel on Climate Change (IPCC), Switzerland, https://www.ipcc.ch/report/2019-refinement-to-the-2006-ipcc-guidelines-for-national-greenhouse-gas-inventories/, published by the IPCC, Geneva, Switzerland, 2019.

Cristofanelli, P., Fontana, I., Tranchida, G., Busetto, M., and Calzolari, F.: Atmospheric CH_4 at Capo Granitola by National Research Council, Institute of Atmospheric Sciences and Climate, https://doi.org/10.50849/WDCGG_0037-6048-1002-01-01-9999, dataset published as CH4_CGR6048_surface-insitu_ISAC_data1, 2025.

Dinoi, A.: Atmospheric CH_4 at Lecce Environmental-Climate Observatory by National Research Council, Institute of Atmospheric Sciences and Climate, https://doi.org/10.50849/WDCGG_0037-6055-1002-01-01-9999, dataset published as *CH4_ECO6055_surface-insitu_ISAC_data1*, 2025.

https://doi.org/10.5194/egusphere-2025-5804
Preprint. Discussion started: 2 February 2026

Dröge, R., van Mil, S., Denier van der Gon, H., Brunner, D., Karstens, U., Wu, Z., Lagergen, F., Scholze, M., Lundblad, M., Witt, H., and van Zanten, M.: Anthropogenic Emission Inventories and Natural Flux Data Sets, Deliverable 2.2, Avengers Project, 2024.

Edwards, D. P., Arellano Jr., A. F., and Deeter, M. N.: A Satellite Observation System Simulation Experiment for Carbon Monoxide in the Lowermost Troposphere, Journal of Geophysical Research: Atmospheres, 114, https://doi.org/10.1029/2008JD011375, 2009.

Forster, P., Storelvmo, T., Armour, K., Collins, W., Dufresne, J.-L., Frame, D., Lunt, D. J., Mauritsen, T., Palmer, M. D., Watanabe, M., Wild, M., and Zhang, H.: The Earth's Energy Budget, Climate Feedbacks, and Climate Sensitivity, in: Climate Change 2021: The Physical Science Basis. Contribution of Working Group I to the Sixth Assessment Report of the Intergovernmental Panel on Climate Change, edited by Masson-Delmotte, V., Zhai, P., Pirani, A., Connors, S. L., Péan, C., Berger, S., Caud, N., Chen, Y., Goldfarb, L., Gomis, M. I., Huang, M., Leitzell, K., Lonnoy, E., Matthews, J. B. R., Maycock, T. K., Waterfield, T., Yelekçi, O., Yu, R., and Zhou, B., pp. 923–1054, Cambridge University Press, Cambridge, United Kingdom and New York, NY, USA, https://doi.org/10.1017/9781009157896.009, 2021.

Heiskanen, J., Brümmer, C., Buchmann, N., Calfapietra, C., Chen, H., Gielen, B., Gkritzalis, T., Hammer, S., Hartman, S., Herbst, M., Janssens, I. A., Jordan, A., Juurola, E., Karstens, U., Kasurinen, V., Kruijt, B., Lankreijer, H., Levin, I., Linderson, M.-L., Loustau, D., Merbold, L., Myhre, C. L., Papale, D., Pavelka, M., Pilegaard, K., Ramonet, M., Rebmann, C., Rinne, J., Rivier, L., Saltikoff, E., Sanders, R., Steinbacher, M., Steinhoff, T., Watson, A., Vermeulen, A. T., Vesala, T., Vítková, G., and Kutsch, W.: The Integrated Carbon Observation System in Europe, https://doi.org/10.1175/BAMS-D-19-0364.1, 2022.

Hersbach, H., Bell, B., Berrisford, P., Hirahara, S., Horányi, A., Muñoz-Sabater, J., Nicolas, J., Peubey, C., Radu, R., Schepers, D., Simmons, A., Soci, C., Abdalla, S., Abellan, X., Balsamo, G., Bechtold, P., Biavati, G., Bidlot, J., Bonavita, M., De Chiara, G., Dahlgren, P., Dee, D., Diamantakis, M., Dragani, R., Flemming, J., Forbes, R., Fuentes, M., Geer, A., Haimberger, L., Healy, S., Hogan, R. J., Hólm, E., Janisková, M., Keeley, S., Laloyaux, P., Lopez, P., Lupu, C., Radnoti, G., de Rosnay, P., Rozum, I., Vamborg, F., Villaume, S., and Thépaut, J.-N.: Complete ERA5 from 1940: Fifth generation of ECMWF atmospheric reanalyses of the global climate, Copernicus Climate Change Service (C3S) Data Store (CDS), https://doi.org/10.24381/cds.143582cf, 2017.

Hersbach, H., Bell, B., Berrisford, P., Biavati, G., Horányi, A., Muñoz Sabater, J., Nicolas, J., Peubey, C., Radu, R., Rozum, I., Schepers, D., Simmons, A., Soci, C., Dee, D., and Thépaut, J.-N.: ERA5 hourly data on single levels from 1940 to present, Copernicus Climate Change Service (C3S) Climate Data Store (CDS), https://doi.org/10.24381/cds.adbb2d47, 2023.

Hoshyaripour, G. A., Baer, A., Bierbauer, S., Bruckert, J., Brunner, D., Foerstner, J., Hamzehloo, A., Hanft, V., Keller, C., Klose, M., Kumar, P., Ludwig, P., Metzner, E., Muth, L., Pauling, A., Porz, N., Reddmann, T., Reißig, L., Ruhnke, R., Satitkovitchai, K., Seifert, A., Sinnhuber, M., Steiner, M., Versick, S., Vogel, H., Weimer, M., Werchner, S., and Hoose, C.: The Atmospheric Composition Component of the ICON modeling framework: ICON-ART version 2025.04, EGUsphere, https://doi.org/10.5194/egusphere-2025-3400, [preprint], 2025.

Hungershoefer, K., Breon, F.-M., Peylin, P., Chevallier, F., Rayner, P., Klonecki, A., Houweling, S., and Marshall, J.: Evaluation of Various Observing Systems for the Global Monitoring of CO_2 Surface Fluxes, Atmospheric Chemistry and Physics, 10, 10 503–10 520, https://doi.org/10.5194/acp-10-10503-2010, 2010.

ICON partnership (DWD and MPI-M and DKRZ and KIT and C2SM): ICON release 2024.01, https://doi.org/10.35089/WDCC/IconRelease01, 2024.

ICOS RI, Bergamaschi, P., Colomb, A., De Mazière, M., Emmenegger, L., Kubistin, D., Lehner, I., Lehtinen, K., Lund Myhre, C., Marek, M., Platt, S. M., Plaß-Dülmer, C., Schmidt, M., Apadula, F., Arnold, S., Blanc, P.-E., Brunner, D., Chen, H., Chmura, L., Conil, S., Couret, C., Cristofanelli, P., Delmotte, M., Forster, G., Frumau, A., Gheusi, F., Hammer, S., Haszpra, L., Heliasz, M., Henne, S., Hoheisel, A., Kneuer, T., Laurila, T., Leskinen, A., Leuenberger, M., Levin, I., Lindauer, M., Lopez, M., Lunder, C., Mammarella, I., Manca, G.,

https://doi.org/10.5194/egusphere-2025-5804
Preprint. Discussion started: 2 February 2026

Manning, A., Marklund, P., Martin, D., Meinhardt, F., Müller-Williams, J., Necki, J., O'Doherty, S., Ottosson-Löfvenius, M., Philippon, C., Piacentino, S., Pitt, J., Ramonet, M., Rivas-Soriano, P., Scheeren, B., Schumacher, M., Sha, M. K., Spain, G., Steinbacher, M., Sørensen, L. L., Vermeulen, A., Vítková, G., Xueref-Remy, I., di Sarra, A., Conen, F., Kazan, V., Roulet, Y.-A., Biermann, T., Heltai, D., Hensen, A., Hermansen, O., Komínková, K., Laurent, O., Levula, J., Pichon, J.-M., Smith, P., Stanley, K., Trisolino, P., ICOS Carbon Portal, ICOS Atmosphere Thematic Centre, ICOS Flask And Calibration Laboratory, and ICOS Central Radiocarbon Laboratory: European Obspack compilation of atmospheric methane data from ICOS and non-ICOS European stations for the period 1984-2024; obspack_ch4_466_GVeu_v9.2_20240502, https://doi.org/10.18160/9B66-SQM1, 2024.

Jähn, M., Kuhlmann, G., Mu, Q., Haussaire, J.-M., Ochsner, D., Osterried, K., Clément, V., and Brunner, D.: An Online Emission Module for Atmospheric Chemistry Transport Models: Implementation in COSMO-GHG v5.6a and COSMO-ART v5.1-3.1, Geoscientific Model Development, 13, 2379–2392, https://doi.org/10.5194/gmd-13-2379-2020, 2020.

Janssens-Maenhout, G., Pinty, B., Dowell, M., Zunker, H., Andersson, E., Balsamo, G., Bézy, J.-L., Brunhes, T., Bösch, H., Bojkov, B., Brunner, D., Buchwitz, M., Crisp, D., Ciais, P., Counet, P., Dee, D., van der Gon, H. D., Dolman, H., Drinkwater, M. R., Dubovik, O., Engelen, R., Fehr, T., Fernandez, V., Heimann, M., Holmlund, K., Houweling, S., Husband, R., Juvyns, O., Kentarchos, A., Landgraf, J., Lang, R., Löscher, A., Marshall, J., Meijer, Y., Nakajima, M., Palmer, P. I., Peylin, P., Rayner, P., Scholze, M., Sierk, B., Tamminen, J., and Veefkind, P.: Toward an Operational Anthropogenic CO2 Emissions Monitoring and Verification Support Capacity, https://doi.org/10.1175/BAMS-D-19-0017.1, 2020.

Kaminski, T. and Rayner, P. J.: Reviews and syntheses: guiding the evolution of the observing system for the carbon cycle through quantitative network design, Biogeosciences, 14, 4755–4766, https://doi.org/10.5194/bg-14-4755-2017, 2017.

Kuenen, J., Dellaert, S., Visschedijk, A., Jalkanen, J.-P., Super, I., and Denier van der Gon, H.: CAMS-REG-v4: A State-of-the-Art High-Resolution European Emission Inventory for Air Quality Modelling, Earth System Science Data, 14, 491–515, https://doi.org/10.5194/essd-14-491-2022, 2022.

Lapenna, E., Buono, A., Mauceri, A., Zaccardo, I., Cardellicchio, F., D'Amico, F., Laurita, T., Amodio, D., Colangelo, C., Di Fiore, G., Gorga, A., Ripepi, E., De Benedictis, F., Pirelli, S., Capozzo, L., Lapenna, V., Pappalardo, G., Trippetta, S., and Mona, L.: ICOS Potenza (Italy) Atmospheric Station: A New Spot for the Observation of Greenhouse Gases in the Mediterranean Basin, Atmosphere, 16, 57, https://doi.org/10.3390/atmos16010057, 2025.

Malacaria, L., Sinopoli, S., Lo Feudo, T., De Benedetto, G., D'Amico, F., Ammoscato, I., Cristofanelli, P., De Pino, M., Gullì, D., and Calidonna, C. R.: Methodology for Selecting Near-Surface CH4, CO, and CO2 Observations Reflecting Atmospheric Background Conditions at the WMO/GAW Station in Lamezia Terme, Italy, Atmospheric Pollution Research, 16, 102 515, https://doi.org/10.1016/j.apr.2025.102515, 2025.

Meirink, J. F., Eskes, H. J., and Goede, A. P. H.: Sensitivity Analysis of Methane Emissions Derived from SCIAMACHY Observations through Inverse Modelling, Atmospheric Chemistry and Physics, 6, 1275–1292, https://doi.org/10.5194/acp-6-1275-2006, 2006.

Miyazaki, K., Maki, T., Patra, P., and Nakazawa, T.: Assessing the Impact of Satellite, Aircraft, and Surface Observations on CO2 Flux Estimation Using an Ensemble-Based 4-D Data Assimilation System, Journal of Geophysical Research: Atmospheres, 116, https://doi.org/10.1029/2010JD015366, 2011.

Nickless, A., Ziehn, T., Rayner, P. J., Scholes, R. J., and Engelbrecht, F.: Greenhouse Gas Network Design Using Backward Lagrangian Particle Dispersion Modelling – Part 2: Sensitivity Analyses and South African Test Case, Atmospheric Chemistry and Physics, 15, 2051–2069, https://doi.org/10.5194/acp-15-2051-2015, 2015.

https://doi.org/10.5194/egusphere-2025-5804
Preprint. Discussion started: 2 February 2026

Park, J. and Kim, H. M.: Design and Evaluation of CO_2 Observation Network to Optimize Surface CO_2 Fluxes in Asia Using Observation System Simulation Experiments, Atmospheric Chemistry and Physics, 20, 5175–5195, https://doi.org/10.5194/acp-20-5175-2020, 2020.

Rayner, P. J., Enting, J. G., and Trudinger, C. M.: Optimizing the CO2 Observing Network for Constraining Sources and Sinks, Tellus B: Chemical and Physical Meteorology, 48, https://doi.org/10.3402/tellusb.v48i4.15924, 1996.

Remaud, M., Chevallier, F., Maignan, F., Belviso, S., Berchet, A., Parouffe, A., Abadie, C., Bacour, C., Lennartz, S., and Peylin, P.: Plant Gross Primary Production, Plant Respiration and Carbonyl Sulfide Emissions over the Globe Inferred by Atmospheric Inverse Modelling, Atmospheric Chemistry and Physics, 22, 2525–2552, https://doi.org/10.5194/acp-22-2525-2022, 2022.

Rieger, D., Bangert, M., Bischoff-Gauss, I., Förstner, J., Lundgren, K., Reinert, D., Schröter, J., Vogel, H., Zängl, G., Ruhnke, R., and Vogel, B.: ICON–ART 1.0 – a New Online-Coupled Model System from the Global to Regional Scale, Geoscientific Model Development, 8, 1659–1676, https://doi.org/10.5194/gmd-8-1659-2015, 2015.

Romano, D., Bernetti, A., Caputo, A., Cordella, M., De Lauretis, R., Di Cristofaro, E., Fiore, A., Gagna, A., Gonella, B., Moricci, F., Pellis, G., Taurino, E., and Vitullo, M.: Italian Greenhouse Gas Inventory 1990-2023. National Inventory Report 2025, Rapporti, 411/25, Istituto Superiore per la Protezione e la Ricerca Ambientale (ISPRA), Rome, Italy, 2024.

Santaren, D., Broquet, G., Bréon, F.-M., Chevallier, F., Siméoni, D., Zheng, B., and Ciais, P.: A Local- to National-Scale Inverse Modeling System to Assess the Potential of Spaceborne CO_2 Measurements for the Monitoring of Anthropogenic Emissions, Atmospheric Measurement Techniques, 14, 403–433, https://doi.org/10.5194/amt-14-403-2021, 2021.

Saunois, M., Stavert, A. R., Poulter, B., Bousquet, P., Canadell, J. G., Jackson, R. B., Raymond, P. A., Dlugokencky, E. J., Houweling, S., Patra, P. K., Ciais, P., Arora, V. K., Bastviken, D., Bergamaschi, P., Blake, D. R., Brailsford, G., Bruhwiler, L., Carlson, K. M., Carrol, M., Castaldi, S., Chandra, N., Crevoisier, C., Crill, P. M., Covey, K., Curry, C. L., Etiope, G., Frankenberg, C., Gedney, N., Hegglin, M. I., Höglund-Isaksson, L., Hugelius, G., Ishizawa, M., Ito, A., Janssens-Maenhout, G., Jensen, K. M., Joos, F., Kleinen, T., Krummel, P. B., Langenfelds, R. L., Laruelle, G. G., Liu, L., Machida, T., Maksyutov, S., McDonald, K. C., McNorton, J., Miller, P. A., Melton, J. R., Morino, I., Müller, J., Murguia-Flores, F., Naik, V., Niwa, Y., Noce, S., O'Doherty, S., Parker, R. J., Peng, C., Peng, S., Peters, G. P., Prigent, C., Prinn, R., Ramonet, M., Regnier, P., Riley, W. J., Rosentreter, J. A., Segers, A., Simpson, I. J., Shi, H., Smith, S. J., Steele, L. P., Thornton, B. F., Tian, H., Tohjima, Y., Tubiello, F. N., Tsuruta, A., Viovy, N., Voulgarakis, A., Weber, T. S., van Weele, M., van der Werf, G. R., Weiss, R. F., Worthy, D., Wunch, D., Yin, Y., Yoshida, Y., Zhang, W., Zhang, Z., Zhao, Y., Zheng, B., Zhu, Q., Zhu, Q., and Zhuang, Q.: The Global Methane Budget 2000–2017, Earth System Science Data, 12, 1561–1623, https://doi.org/10.5194/essd-12-1561-2020, 2020.

Saunois, M., Martinez, A., Poulter, B., Zhang, Z., Raymond, P. A., Regnier, P., Canadell, J. G., Jackson, R. B., Patra, P. K., Bousquet, P., Ciais, P., Dlugokencky, E. J., Lan, X., Allen, G. H., Bastviken, D., Beerling, D. J., Belikov, D. A., Blake, D. R., Castaldi, S., Crippa, M., Deemer, B. R., Dennison, F., Etiope, G., Gedney, N., Höglund-Isaksson, L., Holgerson, M. A., Hopcroft, P. O., Hugelius, G., Ito, A., Jain, A. K., Janardanan, R., Johnson, M. S., Kleinen, T., Krummel, P. B., Lauerwald, R., Li, T., Liu, X., McDonald, K. C., Melton, J. R., Mühle, J., Müller, J., Murguia-Flores, F., Niwa, Y., Noce, S., Pan, S., Parker, R. J., Peng, C., Ramonet, M., Riley, W. J., Rocher-Ros, G., Rosentreter, J. A., Sasakawa, M., Segers, A., Smith, S. J., Stanley, E. H., Thanwerdas, J., Tian, H., Tsuruta, A., Tubiello, F. N., Weber, T. S., van der Werf, G. R., Worthy, D. E. J., Xi, Y., Yoshida, Y., Zhang, W., Zheng, B., Zhu, Q., Zhu, Q., and Zhuang, Q.: Global Methane Budget 2000–2020, Earth System Science Data, 17, 1873–1958, https://doi.org/10.5194/essd-17-1873-2025, 2025.

Savas, D., Dufour, G., Coman, A., Siour, G., Fortems-Cheiney, A., Broquet, G., Pison, I., Berchet, A., and Bessagnet, B.: Anthropogenic NOx Emission Estimations over East China for 2015 and 2019 Using OMI Satellite Observations and the New Inverse Modeling System CIF-CHIMERE, Atmosphere, 14, 154, https://doi.org/10.3390/atmos14010154, 2023.

https://doi.org/10.5194/egusphere-2025-5804
Preprint. Discussion started: 2 February 2026

Schröter, J., Rieger, D., Stassen, C., Vogel, H., Weimer, M., Werchner, S., Förstner, J., Prill, F., Reinert, D., Zängl, G., Giorgetta, M., Ruhnke, R., Vogel, B., and Braesicke, P.: ICON-ART 2.1: A Flexible Tracer Framework and Its Application for Composition Studies in Numerical Weather Forecasting and Climate Simulations, Geoscientific Model Development, 11, 4043–4068, https://doi.org/10.5194/gmd-11-4043-2018, 2018.

Segers, A.: Evaluation and Quality Control Document for Observation-Based CH4 Flux Estimates for the Period 1979-2021, 2022.

Sferlazzo, D., di Sarra, A., Piacentino, S., Di Iorio, T., Monteleone, F., and Anello, F.: Atmospheric CH_4 at Madonie – Piano Battaglia by Italian National Agency for New Technologies, Energy and Sustainable Economic Development, https://doi.org/10.50849/WDCGG_0037-6418-1002-01-01-9999, dataset published as CH4_MDN6418_surface-flask_ENEA_data1, 2025.

Shiga, Y. P., Michalak, A. M., Gourdji, S. M., Mueller, K. L., and Yadav, V.: Detecting Fossil Fuel Emissions Patterns from Subcontinental Regions Using North American in Situ CO2 Measurements, Geophysical Research Letters, 41, 4381–4388, https://doi.org/10.1002/2014GL059684, 2014.

Smith, B., Prentice, I. C., and Sykes, M. T.: Representation of Vegetation Dynamics in the Modelling of Terrestrial Ecosystems: Comparing Two Contrasting Approaches within European Climate Space, Global Ecology and Biogeography, 10, 621–637, https://doi.org/10.1046/j.1466-822X.2001.t01-1-00256.x, 2001.

Steiner, M., Cantarello, L., Henne, S., and Brunner, D.: Flow-Dependent Observation Errors for Greenhouse Gas Inversions in an Ensemble Kalman Smoother, Atmospheric Chemistry and Physics, 24, 12 447–12 463, https://doi.org/10.5194/acp-24-12447-2024, 2024a.

Steiner, M., Peters, W., Luijkx, I., Henne, S., Chen, H., Hammer, S., and Brunner, D.: European CH_4 Inversions with ICON-ART Coupled to the CarbonTracker Data Assimilation Shell, Atmospheric Chemistry and Physics, 24, 2759–2782, https://doi.org/10.5194/acp-24-2759-2024, 2024b.

Super, I., Dellaert, S. N. C., Visschedijk, A. J. H., and Denier van der Gon, H. A. C.: Uncertainty analysis of a European high-resolution emission inventory of CO2 and CO to support inverse modelling and network design, Atmospheric Chemistry and Physics, 20, 1795–1816, https://doi.org/10.5194/acp-20-1795-2020, 2020.

Szénási, B., Berchet, A., Broquet, G., Segers, A., Gon, H. D. V. D., Krol, M., Hullegie, J. J. S., Kiesow, A., Günther, D., Petrescu, A. M. R., Saunois, M., Bousquet, P., and Pison, I.: A Pragmatic Protocol for Characterising Errors in Atmospheric Inversions of Methane Emissions over Europe, Tellus B: Chemical and Physical Meteorology, 73, 1914 989, https://doi.org/10.1080/16000889.2021.1914989, 2021.

Takele Kenea, S., Shin, D., Li, S., Joo, S., Kim, S., and Labzovskii, L. D.: Designing Additional CO2 In-Situ Surface Observation Networks over South Korea Using Bayesian Inversion Coupled with Lagrangian Modelling, Atmospheric Environment, 326, 120 471, https://doi.org/10.1016/j.atmosenv.2024.120471, 2024.

Thanwerdas, J., Saunois, M., Berchet, A., Pison, I., Vaughn, B. H., Michel, S. E., and Bousquet, P.: Variational Inverse Modeling within the Community Inversion Framework v1.1 to Assimilate $\delta^{13}C(CH_4)$ and CH_4: A Case Study with Model LMDz-SACS, Geoscientific Model Development, 15, 4831–4851, https://doi.org/10.5194/gmd-15-4831-2022, 2022a.

Thanwerdas, J., Saunois, M., Pison, I., Hauglustaine, D., Berchet, A., Baier, B., Sweeney, C., and Bousquet, P.: How Do Cl Concentrations Matter for the Simulation of CH_4 and $\delta^{13}C(CH_4)$ and Estimation of the CH_4 Budget through Atmospheric Inversions?, Atmospheric Chemistry and Physics, 22, 15 489–15 508, https://doi.org/10.5194/acp-22-15489-2022, 2022b.

Thanwerdas, J., Saunois, M., Berchet, A., Pison, I., and Bousquet, P.: Investigation of the Renewed Methane Growth Post-2007 with High-Resolution 3-D Variational Inverse Modeling and Isotopic Constraints, Atmospheric Chemistry and Physics, 24, 2129–2167, https://doi.org/10.5194/acp-24-2129-2024, 2024.

https://doi.org/10.5194/egusphere-2025-5804
Preprint. Discussion started: 2 February 2026

Thanwerdas, J., Berchet, A., Constantin, L., Tsuruta, A., Steiner, M., Reum, F., Henne, S., and Brunner, D.: Improving the Ensemble Square Root Filter (EnSRF) in the Community Inversion Framework: A Case Study with ICON-ART 2024.01, Geoscientific Model Development, 18, 1505–1544, https://doi.org/10.5194/gmd-18-1505-2025, 2025.

UNFCCC: The Paris Agreement, http://unfccc.int/files/essential_background/convention/application/pdf/english_paris_agreement.pdf, 25 pp., 2015.

van der Werf, G. R., Randerson, J. T., Giglio, L., van Leeuwen, T. T., Chen, Y., Rogers, B. M., Mu, M., van Marle, M. J. E., Morton, D. C., Collatz, G. J., Yokelson, R. J., and Kasibhatla, P. S.: Global Fire Emissions Estimates during 1997–2016, Earth System Science Data, 9, 697–720, https://doi.org/10.5194/essd-9-697-2017, 2017.

Villalobos, Y., Gómez-Ortiz, C., Scholze, M., Monteil, G., Karstens, U., Fiore, A., Brunner, D., Thanwerdas, J., and Cristofanelli, P.: Towards Improving Top–down National CO2 Estimation in Europe: Potential from Expanding the ICOS Atmospheric Network in Italy, Environmental Research Letters, 20, 054 002, https://doi.org/10.1088/1748-9326/adc41e, 2025.

Villani, M. G., Bergamaschi, P., Krol, M., Meirink, J. F., and Dentener, F.: Inverse Modeling of European CH_4 Emissions: Sensitivity to the Observational Network, Atmospheric Chemistry and Physics, 10, 1249–1267, https://doi.org/10.5194/acp-10-1249-2010, 2010.

Wang, Y., Broquet, G., Ciais, P., Chevallier, F., Vogel, F., Wu, L., Yin, Y., Wang, R., and Tao, S.: Potential of European $^{14}CO_2$ Observation Network to Estimate the Fossil Fuel CO_2 Emissions via Atmospheric Inversions, Atmospheric Chemistry and Physics, 18, 4229–4250, https://doi.org/10.5194/acp-18-4229-2018, 2018.

Wittig, S., Berchet, A., Pison, I., Saunois, M., Thanwerdas, J., Martinez, A., Paris, J.-D., Machida, T., Sasakawa, M., Worthy, D. E. J., Lan, X., Thompson, R. L., Sollum, E., and Arshinov, M.: Estimating Methane Emissions in the Arctic Nations Using Surface Observations from 2008 to 2019, Atmospheric Chemistry and Physics, 23, 6457–6485, https://doi.org/10.5194/acp-23-6457-2023, 2023.

Wu, L., Broquet, G., Ciais, P., Bellassen, V., Vogel, F., Chevallier, F., Xueref-Remy, I., and Wang, Y.: What Would Dense Atmospheric Observation Networks Bring to the Quantification of City CO_2 Emissions?, Atmospheric Chemistry and Physics, 16, 7743–7771, https://doi.org/10.5194/acp-16-7743-2016, 2016.

Yu, X., Millet, D. B., and Henze, D. K.: How Well Can Inverse Analyses of High-Resolution Satellite Data Resolve Heterogeneous Methane Fluxes? Observing System Simulation Experiments with the GEOS-Chem Adjoint Model (V35), Geoscientific Model Development, 14, 7775–7793, https://doi.org/10.5194/gmd-14-7775-2021, 2021.

Zängl, G., Reinert, D., Rípodas, P., and Baldauf, M.: The ICON (ICOsahedral Non-hydrostatic) Modelling Framework of DWD and MPI-M: Description of the Non-Hydrostatic Dynamical Core, Quarterly Journal of the Royal Meteorological Society, 141, 563–579, https://doi.org/10.1002/qj.2378, 2015.

Ziehn, T., Nickless, A., Rayner, P. J., Law, R. M., Roff, G., and Fraser, P.: Greenhouse Gas Network Design Using Backward Lagrangian Particle Dispersion Modelling − Part 1: Methodology and Australian Test Case, Atmospheric Chemistry and Physics, 14, 9363–9378, https://doi.org/10.5194/acp-14-9363-2014, 2014.